C: Surfaces, Interfaces, Porous Materials, and Catalysis

CO-PROX Reaction over CoO|AlO Catalysts – Impact of the Spinel Active Phase Faceting on the Catalytic Performance

Gabriela Grzybek, Klaudia Ciura, Joanna Grybo#, Paulina Indyka, Arantxa Davó-Quiñonero, Dolores Lozano-Castello, Agustín Bueno-López, Andrzej Kotarba, and Zbigniew Sojka

J. Phys. Chem. C, **Just Accepted Manuscript** • DOI: 10.1021/acs.jpcc.9b03025 • Publication Date (Web): 08 Jul 2019

CO-PROX Reaction over $Co_3O_4|Al_2O_3$ Catalysts – Impact of the Spinel Active Phase Faceting on the Catalytic Performance

Gabriela Grzybek[a], Klaudia Ciura[a], Joanna Gryboś[a], Paulina Indyka[a], Arantxa Davó-Quiñonero[b], Dolores Lozano-Castelló[b], Agustin Bueno-Lopez[b], Andrzej Kotarba[a], Zbigniew Sojka[a]*

[a]Faculty of Chemistry, Jagiellonian University, Gronostajowa 2, 30-387 Krakow, Poland

[b]Department of Inorganic Chemistry, University of Alicante, Carretera de San Vicente s/n, Alicante, Spain

*Corresponding Author: Gabriela Grzybek,

e-mail: g.grzybek@uj.edu.pl, phone number: +48 12 686 24 93

ABSTRACT: A series of α-alumina supported cobalt spinel catalysts of various exposition of the (100), (111) and (110) planes was synthetized and tested in CO-PROX reaction.

Successful control of the polyhedral shape of the nano-spinel active phase was achieved via glycerol and/or Zn additions to the impregnation solution. This allowed for the application of such catalysts for resolving the shape-reactivity relationships in a more controlled fashion in comparison to previous studies, where various catalysts of entirely unlike origin were used. The catalysts were thoroughly characterized by means of XRF, XRD, XPS, Raman Spectroscopy, STEM, TPR techniques. The CO-PROX catalytic performance of the obtained catalysts was examined in the TPSR mode. A strong impact of the spinel nanograins morphology on the activity was observed, with the (100) termination found as the most active among the all exposed low index (111) and (110) planes. Furthermore, a linear correlation between the abundance of the surface Co^{3+} cations and the yield of carbon monoxide oxidation reveals their vital relevance as the catalytically CO-PROX active sites. The results are discussed in terms of a thermodynamic diagram of the surface oxygen, water and oxygen vacancy stabilities on the Co_3O_4 most abundant planes, providing the rational background for the superior behavior of the (100) termination in the CO-PROX reaction. The obtained results speak in favor of the involvement of the suprafacial oxygen species in the CO oxidation process.

1. INTRODUCTION

The Preferential Oxidation of CO (CO-PROX) is a catalytic route for purification of H_2 streams produced by steam reforming processes. Most of the CO by-product is consumed in the water-gas shift reaction (WGSR) down to the level of 1% of the feed. Then, the residual content of CO present in the H_2-rich flow can be selectively oxidized in the PROX process. The removal of carbon monoxide, which is considered as a poisoning agent in several applications involving hydrogen reactant, such as ammonia production or fuel cell technologies, must be carried down to the accepted tolerance level, typically around 100 ppm of CO or even below.[1,2] Over the last decades, wide-ranging investigations have been conducted in order to understand the mechanistic course of this process, and optimize the PROX catalysts performance.[3,4] Therefore, tuning the surface redox properties related to the facile generation of selective reactive oxygen species at the catalyst surface is an important aspect of the CO-PROX reaction optimization.[5–7]

So far, catalytic systems containing noble metals deposited on various supports, such as Pt/Al_2O_3,[8–10] Pd/zeolites,[11] Ru/Al_2O_3[12] have been investigated intensively in the CO-PROX reaction. Catalysts based on gold nanoparticles exhibit also high activity in CO oxidation. However, in this case, the PROX process involves different mechanism than for other noble metals.[13–15] The transitions metals (Co, Cu, Ni) supported on oxide carriers (CeO_2, CeO_2–ZrO_2) ,[16–18] which are active in CO oxidation, and transition metal oxides such as supported cobalt spinels Co_3O_4-CeO_2 and Co_3O_4/Al_2O_3[19–21] have been studied as potential CO-PROX catalysts as well. One of the most efficient system in this group of catalytic materials is the benchmarking CuO/CeO_2 system, owing to the remarkable oxygen-storing/releasing capacity of ceria.[22–24]

In this context application of nanostructured catalysts of defined morphology, particle size and faceting (exposure of particular crystallographic planes) in model PROX investigations may

provide valuable information for the rational design of highly selective and catalytically active centers. Bulk transition metal oxides, such as copper or cobalt oxides have been widely examined owing to their high activity.[25,26] In the particular case of cobalt catalysts, Co_3O_4 spinel exhibits a promising catalytic CO-PROX performance.[27,28] However, due to difficulties in the manufacturing of the cobalt spinel catalysts in the form of extrudates, deposition of the spinel active phase on the shaped carriers such as alumina or cordierite is a common practice for large scale applications.[29] It has been found that the alpha polymorph of Al_2O_3 support is the most suitable for the Co_3O_4 dispersion, and leads to the development of preferential spinel nanocrystal morphology, as documented elsewhere.[30] Furthermore, the modification of the spinel deposition method by glycerol addition results in better dispersion and a favored exposition of the preferred active facets. The presence of glycerol in the impregnation mixture changes the spinel crystallites morphology by decreasing the exposition of the less active (111) planes and increasing the abundance of the more active (100) facets.

The previously reported high CO oxidation activity of cobalt spinel has been assigned to the presence of (011) and (112) planes exposed by nanosheets and nanobelts, respectively.[31–33] However, as discussed in the Supporting Information such assignment of the crystal terminations is not univocal. Indeed, in more recent CO-PROX studies of Khasu et al.,[34] using nanocubes, nanobelts, and nanosheets deposited on a silica support, the (100) facet has been advanced as being the most active one. Such discrepancies were probably caused, among others, by poorly defined morphology of the nanosheets and nanobelts used as catalysts, which actually have been identified as superstructures constituted by much smaller crystallites of an obscure faceting.

In order to resolved those discrepancies and to establish the most active termination of cobalt spinel in a definite way, we have examined the CO-PROX process on a uniform type of Co_3O_4 catalyst supported on alumina, where the polyhedral shape of the spinel nanoparticles was tailored by

glycerol addition to the impregnation solution and/or by non-redox Zn-dopin.[35] This allows for controlled variation of the (100), (111) and (110) faceting, while preserving the overall polyhedral shape and size of the spinel active phase nanocrystals. It is worth emphasizing that, in contrast to previous literature, the catalysts used in these investigations are not model single nanocrystals but real supported catalysts applicable on a large scale.[36] The details on the manufacture and multiscale characterization from the nanometric size of active phase grains into centimetre extrudates of these catalysts we have published elsewhere.[30,37,38] To our best knowledge, there is no similar supported real catalytic systems, where the facets abundance has been directly associated with the catalytic CO-PROX behavior.

2. EXPERIMENTAL

2.1 .Catalyst preparation

The series of alpha alumina supported spinel catalysts (Table 1) was prepared. The alpha alumina support, obtained from commercial powder pseudoboehmite (Sasol Versal) by calcination at 1400°C for 4h, was delivered by the New Chemical Synthesis Institute (Puławy, Poland). The spinel active phase was deposited on the alumina support by incipient wetness impregnation using an aqueous or a water-glycerol (30%vol. of glycerol) solution of $Co(NO_3)_2 \cdot 6H_2O$ and $Zn(NO_3)_2 \cdot 6H_2O$ (Sigma Aldrich, 98%) with an appropriate concentration to obtain the spinel (Co_3O_4 or $Co_{2.6}Zn_{0.4}O_4$) content of 10 wt.%. The samples were next dried at 100°C for 12 h, and calcined in air at 500°C for 4 h to obtain a series of $Co_3O_4|Al_2O_3$, $Co_{2.6}Zn_{0.4}O_4|Al_2O_3$ (glycerol-free synthesis) and $Co_3O_4|Al_2O_3$-gly $Co_{2.6}Zn_{0.4}O_4|Al_2O_3$-gly (glycerol-assisted synthesis) catalysts. The calcination at 500°C ensured no carbonaceous impurities in the catalysts, what was confirmed by analysis of TG results and microscopic observation presented previously. [30] A more detailed

description of the catalyst preparation including information about the pore volume of the support, distribution of the particle size alumina support and spinel active phase, loading, composition etc. can be found in our previous papers.[30,39]

2.2 *Characterization methods*

The chemical composition of the samples was determined by means of Energy-Dispersive XRF spectrometer (Thermo Scientific, ARL QUANT'X). The X-rays of 4-50 kV (1 kV step) with the beam size of 1 mm generated by the Rh anode. The detector used was a 3.5 mm Si(Li) drifted crystal with the Peltier cooling (~ 185 K). For quantitative analysis, the calibration with a series of metallic standards and the UniQuant software were used.

X-ray patterns were recorded with a Bruker D8-advance diffractometer, using CuKα radiation (λ= 1.540598 Å). The diffractograms were recorded for 2θ in the range of 10° - 80° with a step of 0.02°, and a time of 3 s per step. The Raman spectra recorded at room temperature in ambient conditions were obtained using a Renishaw InVia spectrometer equipped with a Leica DMLM confocal microscope and a CCD detector with the excitation wavelength of 785 nm. The Raman scattered light was collected in the spectral range of 100–800 cm^{-1} with a resolution of 1 cm^{-1}. At least five scans were accumulated to ensure a sufficient signal to noise ratio. Temperature Programmed Reduction experiments with H_2 (H_2-TPR) were performed using a Micromeritics Pulse ChemiSorb 2705 device. For measurements, 40 mg samples were placed in a U-shaped quartz reactor and the temperature was increased from room temperature up to 950ºC with a heating rate of 10ºC/min in 40 ml/min of 5% H_2 in Ar.

The X-ray photoelectron spectra (XPS) were measured with a Prevac photoelectron spectrometer equipped with a hemispherical VG SCIENTA R3000 analyzer. The spectra were recorded using a monochromatized AlKα source (E = 1486.6 eV) and an electron flood gun (FS40A-PS) to

compensate the residual charge on the surface. The background pressure in the chamber during the measurements was 5×10^{-9} mbar. The spectra were recorded with a pass energy of 100 eV for the survey and narrow scans. All the binding energies were referenced to the C 1s peak at 285 eV of the adventitious carbon. The spectra were fitted with Casa XPS software.

Scanning transmission electron microscopy (STEM) measurements, were carried out using a Tecnai Osiris instrument (FEI) with X-FEG Schottky field emitter operated at accelerating voltage of 200 kV to evaluate the morphology of spinel nanoparticles deposited on the alpha alumina support. The Z-contrast imaging was performed using a High Angle Annular Dark Field (HAADF) detector, and the camera length was kept in the range 330–550 mm, to maximize the signal intensity. Samples for STEM characterization were ultrasonically dispersed in ethanol, dropped into a lacey carbon-coated copper grid (Agar Scientific, 300 mesh), and then dried at room temperature.

The cobalt spinel particle size analysis was performed using the DigitalMicrograph (Gatan) software.[40] The nanocrystals shape retrieving was based on gradient analysis of the HAADF STEM images according to the procedure successfully applied for the supported cobalt spinel catalysts.[30] The procedure is based on *Z*-contrast analysis using calibrated HAADF STEM images, and involves quantification of the relation between the HAADF STEM image intensity and the specimen thickness, followed by image gradient analysis to retrieve the diagnostic shape features (edge pattern). The analysis was performed by employing the Canny algorithm[41] implemented in the FeatureJ[42] software as a part of the image processing ImageJ package[43]). The determined edge pattern provided the local orientation of the observed nanocrystals and was used for assigning the (*x, y*) coordinates of the identified vertices in the observed 2D images. Completed by default values of the lacking *z* coordinates, they were used as an input for the convex hull algorithm to obtain the tentative polyhedral shape of the nanocrystal, taking into account constraints imposed by the spinel

crystal symmetry. The imaging conditions were adjusted in such a way that the image contrast originated mainly from the changes in the thickness of the examined nanocrystals. Finally, by combining the knowledge about the sample structure with the information about the observed edge pattern and variation of the sample thickness, it was possible to retrieve the shape of nanocrystals by using a reversed Wulff construction.[44]

Stability diagram (γ/J·m^{-2} vs. T) of the Co_3O_4 (100) and (111) terminations for bare, oxygen defected and covered with reactive oxygen species (ROS) was constructed using surface energy values obtained from *ab – initio* thermodynamic and DFT modelling, previously published by us elsewhere.[45–48] The changes of H_2O, CO coverages with temperature and the actual partial pressures in the course of the CO-PROX reaction were calculated by employing a multisite Langmuir isotherm for water and carbon oxide sorption on the cobalt spinel facets of interest.[49]

2.3 Catalytic tests

The catalytic tests were carried out in a U-shaped fix-bed quartz reactor with 16 mm inner diameter coupled to a gas chromatograph (HP model 6890 Plus Series) equipped with two columns: Porapak Q 80/100 for CO_2 and H_2O separation and Molecular Sieve 13X for O_2 and CO separation. The gas feed (2% CO, 2% O_2, 30% H_2 with He balance in a total) flow rate of 100 ml/min was set by means of Mass Flow Controllers (Bronkhorst). The O_2 excess with regard to CO was equal to λ = 2 (for stoichiometric CO-O_2 conditions λ = 1). The catalytic measurements were performed with 150 mg of catalyst, using the heating rate of 2ºC/min from 25 to 225ºC. To ensure that the reactor is operating in the kinetic regime, the criterial numbers for extra- and intra-granular diffusion limitations were checked according to the EUROKIN[50] procedure (see ESI, Table S3). In order to check reproducibility of the catalytic results and stability of the samples in CO-PROX reaction conditions, 3 consecutive cycles of reaction were conducted.

3. RESULTS AND DISCUSSION

3.1 Characterization of the synthesized catalysts

The investigated alumina supported spinel catalysts were characterized with respect to the active phase loading (XRF), spinel active phase structure (XRD, Raman Spectroscopy), catalysts morphology (STEM observations combined with the reversed Wulff construction) and surface composition (XPS). Characterization of the catalysts was complemented by temperature programmed reduction (H_2 – TPR) experiments. The elemental composition of the samples determined from XRF analysis confirmed that the desired loading of the spinel active phase of about 10 wt.% was achieved (Table 1).

Table 1. The surface area and cobalt spinel content (XRF) of the investigated samples.

Sample	Surface area/ $m^2 \cdot g^{-1}$	Co_3O_4 content/%
$Co_3O_4\|Al_2O_3$	5	9.2
$Co_3O_4\|Al_2O_3$-gly	11	10.5
$Co_{2.6}Zn_{0.4}O_4\|Al_2O_3$	8	8.9
$Co_{2.6}Zn_{0.4}O_4\|Al_2O_3$-gly	12	10.8

The crystalline structure of the studied catalysts was investigated by both XRD and micro-Raman techniques. The obtained X-ray diffraction patterns are collated in Figure 1.

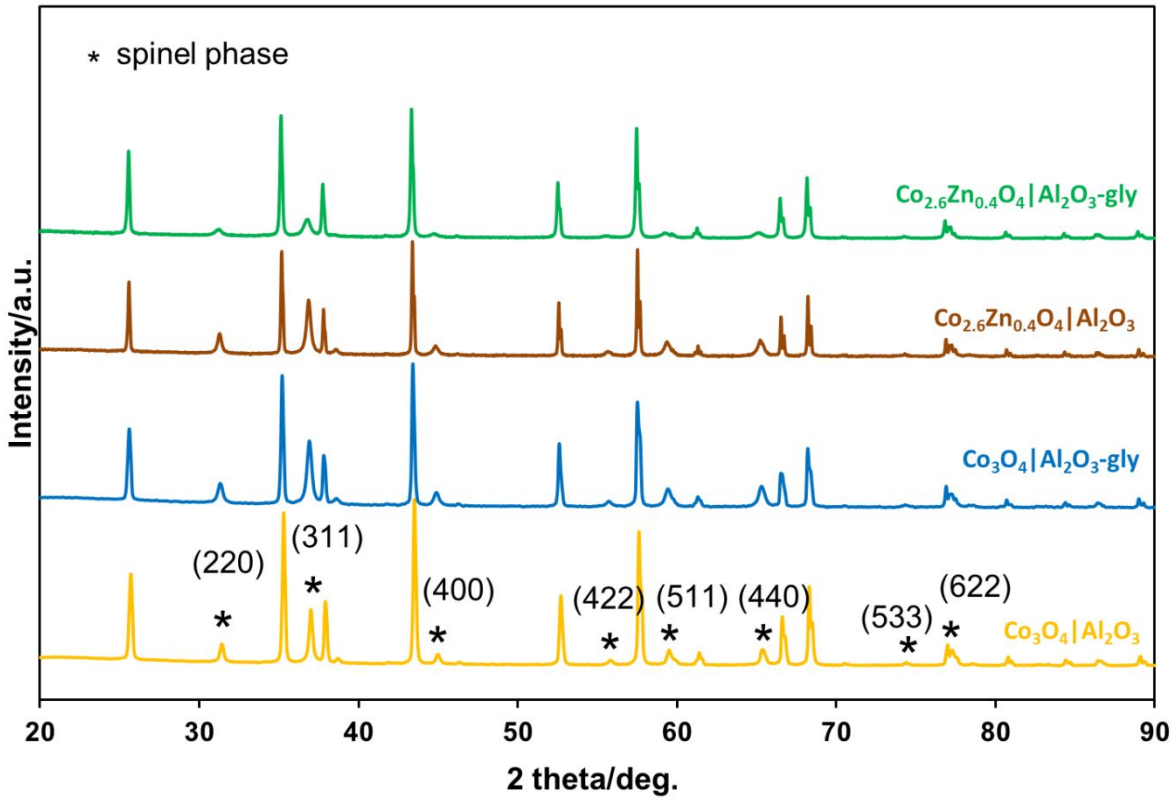

Figure 1. The X-ray diffraction patterns of the examined alumina supported spinel catalysts.

The diffraction lines at $2\Theta = 25.6$; 35.1; 37.7; 43.4; 52.5; 57.5; 59.4; 61.2; 66.5 and 68.2 correspond to (012), (104), (110), (113), (024), (116), (211), (122), (214) and (300) planes of the α-Al_2O_3 support, respectively, indexed within the R-3c space group (ICSD – 9771). Formation of the spinel cobalt oxide upon decomposition of the various precursors used was revealed by the presence of the characteristic lower intensity lines (marked by * in Fig. 1) that appear at $2\Theta = 31.3$; 36.9; 44.9; 55.6; 59.5; 65.4, 74.4 and 77.3, and correspond to the (220), (311), (400), (422), (511), (440), (533) and (622) reflection planes of Co_3O_4 (ICSD – 69378), respectively. The Raman spectra of the studied catalysts are collated in Figure 2.

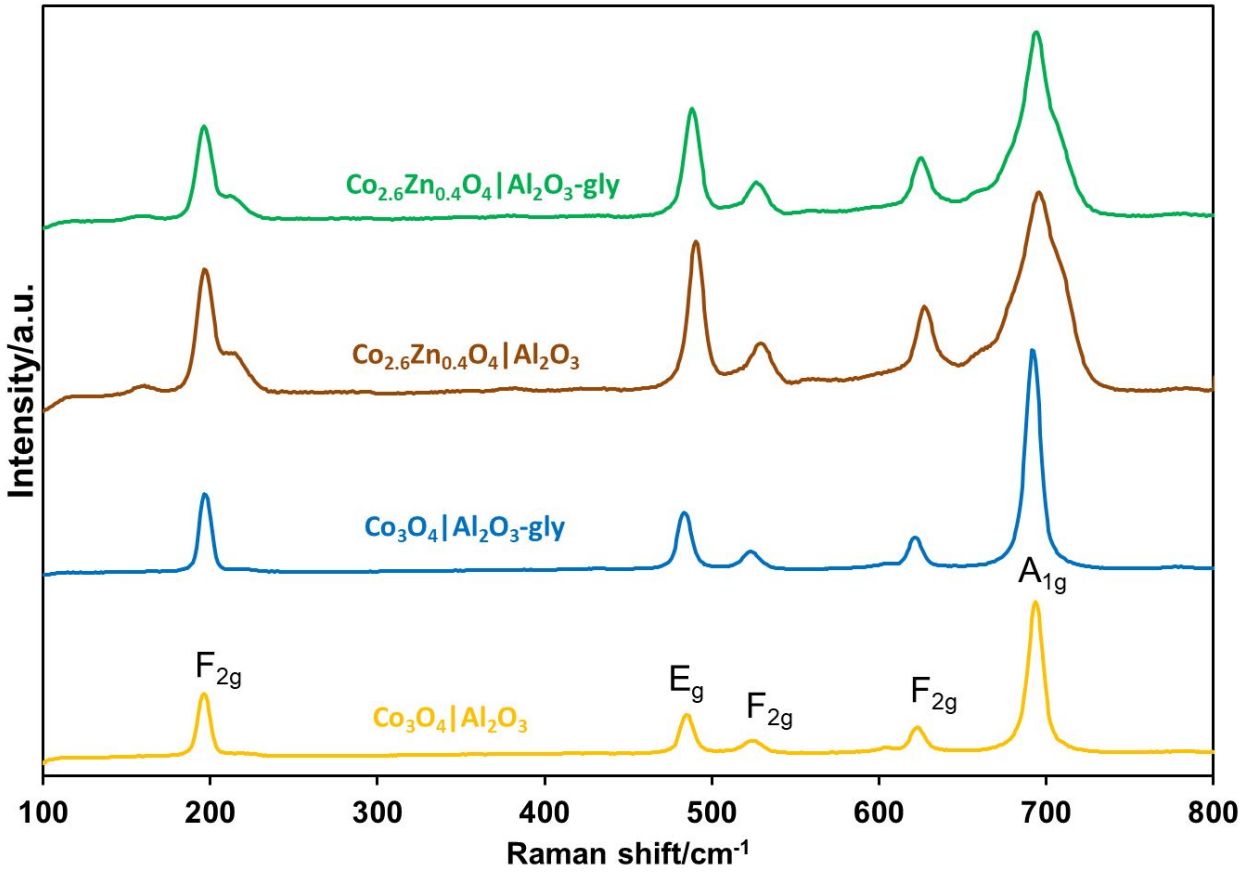

Figure 2. The Raman spectra of the synthetized alumina supported spinel catalysts.

In all cases, the five diagnostic F_{2g}, E_g, F_{2g}, F_{2g} and A_{1g} vibrational modes of cobalt spinel,[51] located at 198, 486, 527, 625 and 694 cm^{-1}, respectively, are present. The observed asymmetry and broadening of the F_{2g} (195 cm^{-1}) and A_{1g} (694 cm^{-1}) peaks, observed in the case of the samples doped with zinc, imply formation of the intended mixed Co-Zn spinel as previously reported elsewhere.[36] More important, the XRD and Raman investigations confirmed the lack of undesired segregation of ZnO from the spinel active phase (confirmed additionally by STEM-EDX elemental mapping, see below).

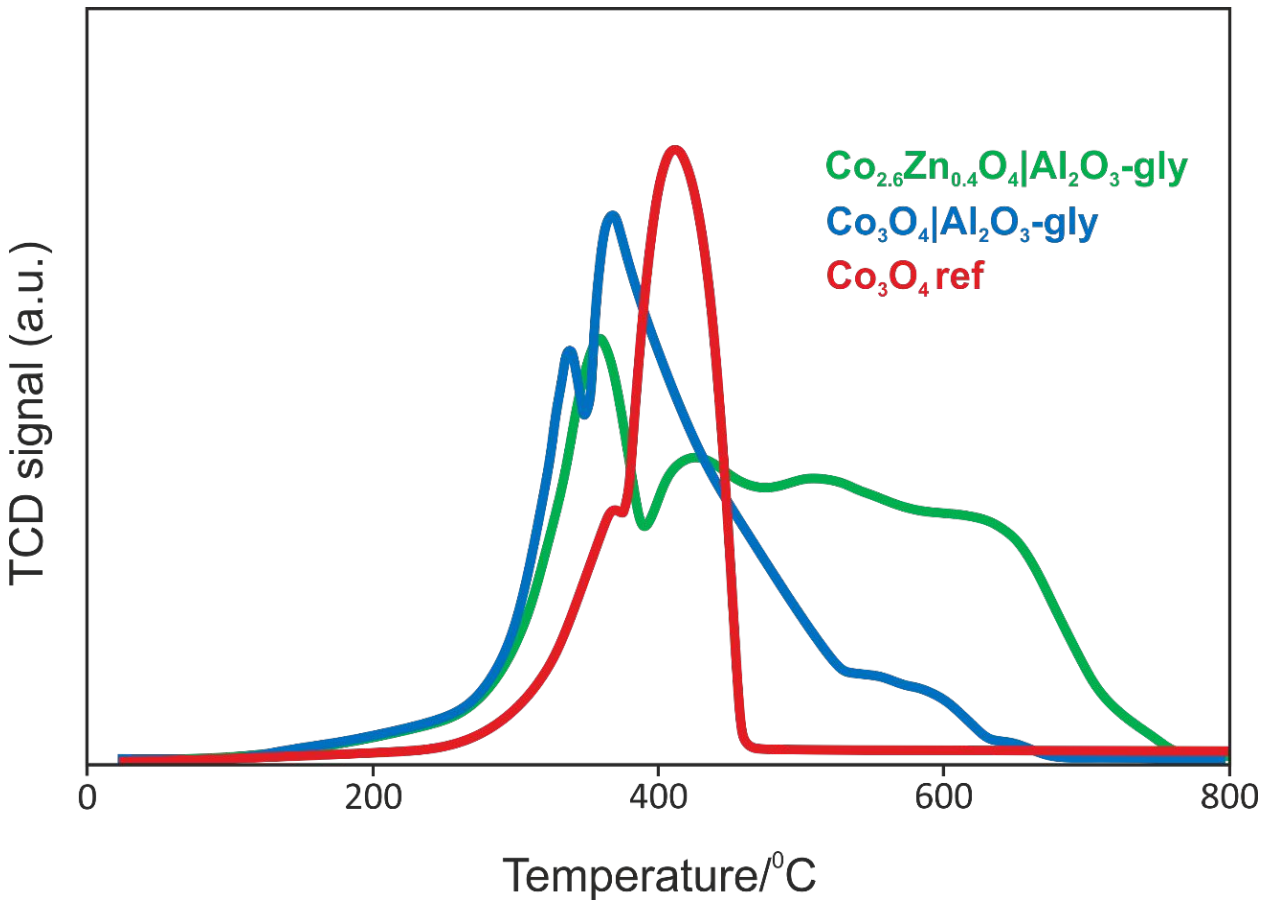

Figure 3. H_2-TPR profiles of alumina supported and bare Co_3O_4 (reference) catalysts obtained in various way (Note: TCD signal for Co_3O_4 reference sample was divided by 20 for the sake of clarity in the qualitative comparison of the reduction profiles).

The XRD and Raman spectroscopic characterization of the catalysts was complemented by temperature programmed reduction experiments (H_2-TPR). The observed reduction profiles of the examined samples are presented in Figure 3.

Typically, for the reference bulk Co_3O_4 spinel, the TPR profile consists of two main reduction processes, associated with a reduction of the octahedral Co^{3+} cations into Co^{2+} at a lower temperature,

$$(Co^{2+})[Co^{3+}Co^{3+}O_4] + xH_2 \rightarrow (Co^{2+}{}_{1-x})[Co^{3+}{}_{2-2x}Co^{2+}{}_{3x}O_{4-x}] + xH_2O \qquad 0 \le x \le 1$$

followed by reduction of the resultant Co^{2+} cations (in the formed CoO) into segregated metallic cobalt at higher temperatures,

$$3(Co^{2+}O) + xH_2 \rightarrow (Co^{2+}O)_{3-x}|Co + xH_2O \qquad 0 \le x \le 3$$

as discussed in detail elsewhere.[52] Dispersion of cobalt spinel particles onto inert alumina support affects significantly the main scenario of the reduction process, despite that in the XRD and Raman characterization of the samples no traces of Co-Al mixed spinel formation were detected.

Thus, in the case of the $Co_3O_4|Al_2O_3$-gly catalyst, the two major reduction peaks, centered at 338 and 366ºC, respectively, are in general compatible with the bulk Co_3O_4 reduction profile. However, the first peak is shifted towards lower temperatures as dispersion facilitates the accessibility of the reduction centers. The high-temperature Co^{2+} reduction band is, in turn, markedly extended toward higher temperatures. The tailing is even more pronounced in the case of the $Co_{2.6}Zn_{0.4}O_4|Al_2O_3$-gly sample. Such broadening of the reduction profile may be associated with steady changes in the solid state status of zinc in the nascent CoO produced upon the reduction progress, resulting from gradual segregation of the metallic cobalt in the late stages of the reduction process. Although the overall TPR curves of the $Co_{2.6}Zn_{0.4}O_4|Al_2O_3$-gly and $Co_3O_4|Al_2O_3$-gly sample are clearly different, the onset shapes of the reduction curves are rather similar. The observed TPR profiles show that the trivalent cobalt reduction is quite facile, whereas divalent cobalt reduction is significantly hindered upon dispersion on alumina. This behavior may be beneficial for PROX

application, stabilizing the catalyst against a harmful over-reduction. Furthermore, since the optimal temperature window for CO-PROX reaction is in the range 120 - 200°C (see Fig. 3), the TPR results imply that only the redox changes of Co^{3+} cations are relevant. The lower reducibility of the cobalt-based catalyst has been associated previously with better catalytic performance in CO oxidation, being indicative of higher average redox state of cobalt, and larger stabilization of oxidized species,[53] this conjecture is, however, not supported in our case. A particle size dependence of the reduction/re-oxidation of cobalt spinel has been thoroughly examined by us previously,[52] and it has been documented that the TPR/TPO results can be rationalized by means of size-dependent Ellingham diagrams ($\log(pO_2/p^0)$ vs T).

The STEM images (Fig. 4) show the particles of cobalt (b, d) and mixed Co-Zn (a, c) spinels that were deposited on the much larger grains of the α-Al_2O_3 carrier. Closer inspection of the STEM results reveals the presence of the spinel nanocrystals of various morphology, size, and agglomeration extent, decorating the blunt micrometer-size particles of the alumina support. Yet, the majority of the investigated spinel nanocrystals exhibit morphology, which strongly depends on the catalyst synthesis method. In order to get a more clear insight into the shape of the spinel active phase nanocrystals, appropriate digital image post-processing of the obtained images is required. It involves the transformation of the parent images into their gradient representations, which is more sensitive to the topographic features associated with the abrupt changes of the image contrast. The results of such comprehensive shape analysis of the STEM images combined with the inversed Wulff construction for each sample is presented in Figure 5.

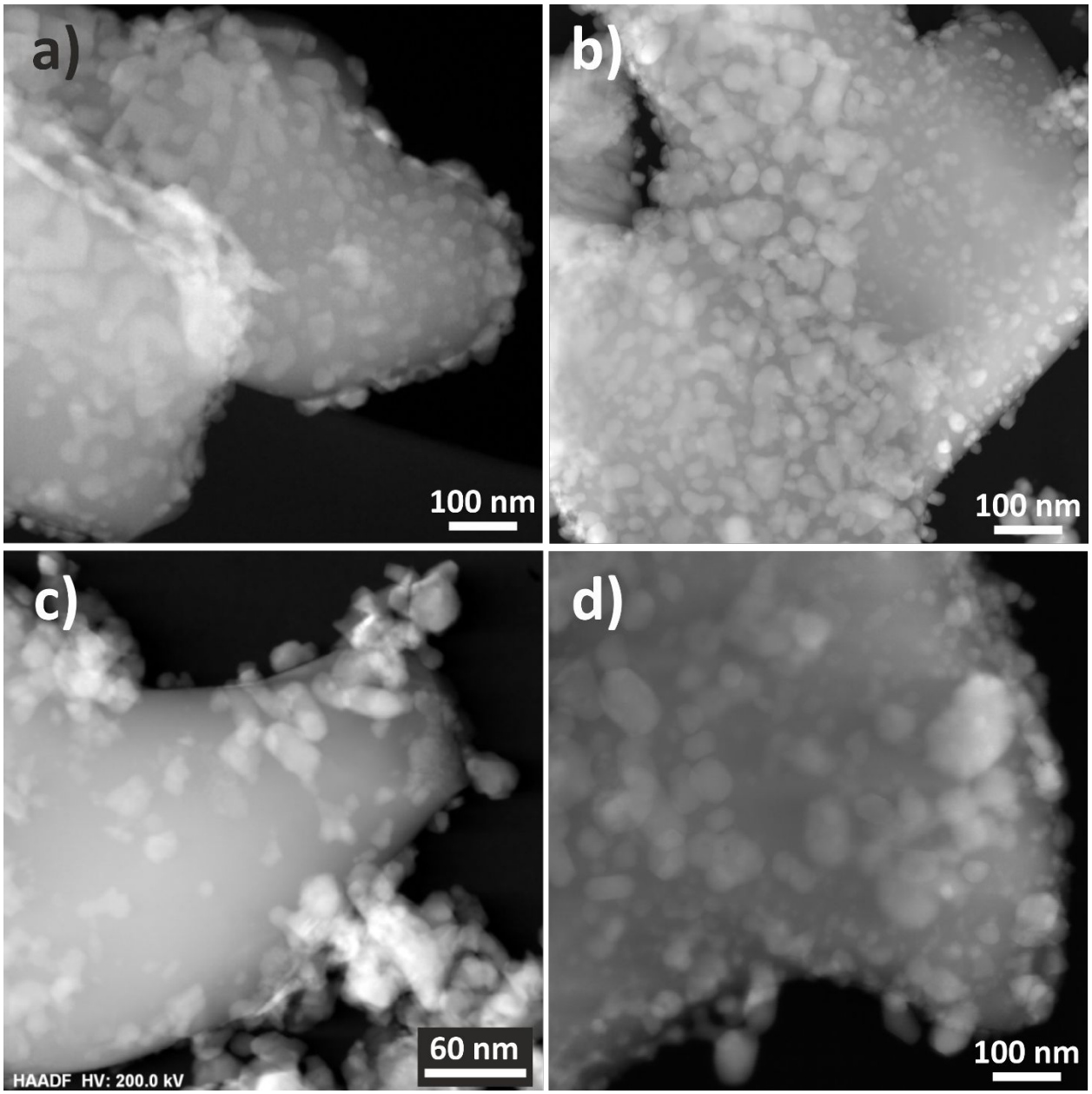

Figure 4. STEM survey images of the investigated catalysts (a) $Co_{2.6}Zn_{0.4}O_4|Al_2O_3$–gly, (b) $Co_3O_4|Al_2O_3$–gly, (c) $Co_{2.6}$ $Zn_{0.4}O_4|Al_2O_3$, (d) $Co_3O_4|Al_2O_3$.

It should be noted that for the shape analysis nanocrystals of different sizes were selected in order to take into account the size effect intrinsically. Therefore, the presented assessment of the facets

abundance includes both shape and size variation effects. Such procedure has been successfully applied for evaluation of the faceting for Mn-Co spinels dispersed over carbon support.[54]

The panel presented in Figure 5 has the following structure: the left column corresponds to the original HAADF STEM pictures ($a_1 – d_1$), the next column presents their gradient version with the intensity line scans in the region of interest ($a_2 – d_2$), followed by two columns showing the gradient representation with the superimposed Wulff hulls ($a_3 – d_3$), and the retrieved idealized (flat surface) spinel nanocrystal shapes ($a_4 – d_4$). The right column presents the abundance of each facet in the retrieved polyhedra ($a_5 – d_5$). For the properly adjusted imaging conditions, the intensity of the HAADF STEM image depends only on the atomic number *Z* and the thickness of the nanocrystal (average number of the atoms in the projected columns). This provides the bases for determination of the individual nanocrystal shape from the computer analysis of the projected shape and the contrast distribution profiles. Application of gradient representation of the microscopic images emphasizes the edge pattern of the examined nanocrystals projected on the viewing plane. The local orientation of the nanocrystals was assessed by the analysis of the interfacial angles, which are preserved even for the malformed nanocrystals (Steno law). The lack of the contrast gradient, in turn, indicates the constant thickness of the examined nanocrystal fragment without changes in the faceting. Despite non-perfect polyhedral morphologies, the characteristic values of the interfacial angles allowed for reliable assignment of the exposed planes. An example of such analysis of the interfacial angles is shown in the first column ($a_1 – d_1$). Combining this information together with the constraints imposed by the spinel crystallographic structure it was possible to retrieve the model polyhedral shape of the observed nanocrystals by adjusting properly oriented Wulff hulls to the experimental edge patterns. Typical results of such examination of the microscopic images are presented in Fig. 5, and further examples are provided in Supporting Information in Figs. S1-S4.

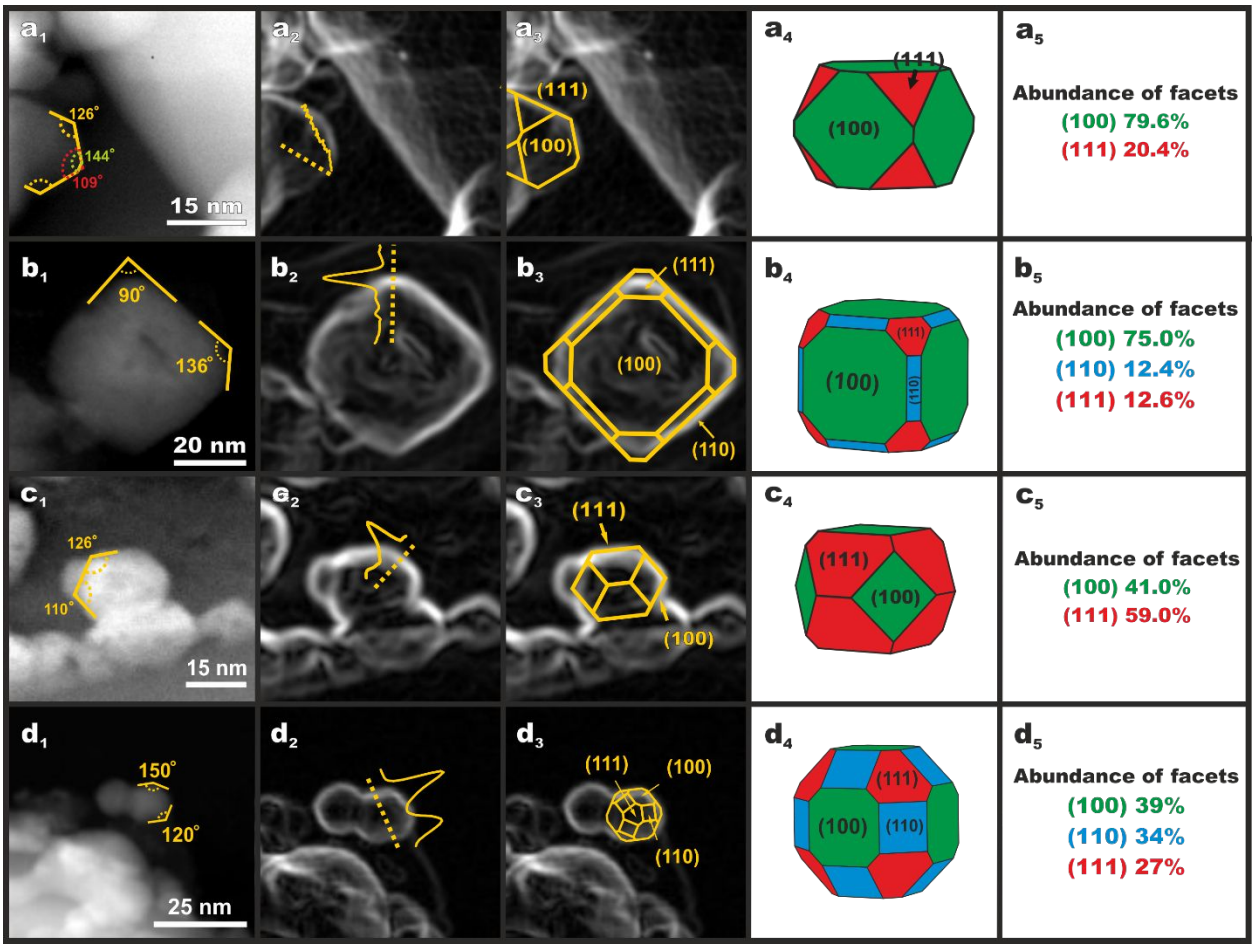

Figure 5. HAADF/STEM images of the investigated samples: a_1 – b_1) zinc - cobalt spinel and cobalt spinel deposited on α-Al_2O_3 support, obtained by impregnation with glycerol solution ($Co_{2.6}Zn_{0.4}O_4|Al_2O_3$-gly, $Co_3O_4|Al_2O_3$-gly) c_1 – d_1) zinc - cobalt spinel and cobalt spinel deposited on α-Al_2O_3 support, obtained by impregnation with aqueous solution ($Co_{2.6}Zn_{0.4}O_4|Al_2O_3$, $Co_3O_4|Al_2O_3$), along with the shape retrieval by means of the inverse Wulff construction a_2 – d_4) relative abundance of the exposed facets (a_5 – d_5).

In the case of the $Co_{2.6}Zn_{0.4}O_4|Al_2O_3$-gly nanocrystals (Fig. 5 a_1–a_5) the projected contours (Fig. 5 a_1) have the interplanar angles close to 125°, 145° and 109°, which according the crystallographic constraints can be assigned to the intersection of the following pairs of the facets: (111)/(100), (111)/(110) and (111)/(111), respectively. The analysis of the image gradient revealed that the image intensity decreases monotonically from the edges towards the center of the nanocrystal, indicating constant changes in the thickness along the (100) facet, which is tantamount with the presence of a single plane (Fig. 5 a_2). Hence, by combining the identified pairs of the intersecting facets with the contrast gradient analysis along the nanocrystal projection, a cuboctahedral shape of the nanocrystal was retrieved. The analyzed example of the cuboctahedral nanocrystal exhibits the following abundance of the facets: 79.6% - (100); 20.4% - (111) (Fig 5 a_4 _ a_5). Examination of a large population of the nanocrystals revealed that such morphology is representative for the prevailing amount of the nanocrystals present in the sample with the estimated error of about 10%. We may then conclude that the cobalt-zinc spinel nanocrystals obtained by impregnation with glycerol solution are characterized by preferential exposure of the (100) facet (> 70%). An analogous procedure was applied for the shape retrieval for the remaining samples. Representative results gauging the abundance of the facets for the $Co_3O_4|Al_2O_3$-gly, $Co_{2.6}Zn_{0.4}O_4|Al_2O_3$ and $Co_3O_4|Al_2O_3$ nanocrystals are presented in column b_5 – d_5 (Fig 5). The morphology of the $Co_3O_4|Al_2O_3$-gly grains is again characterized by preferential exposure of the (100) facet, however, its contribution is reduced in comparison to the $Co_{2.6}Zn_{0.4}O_4|Al_2O_3$-gly catalyst. In the case of the cobalt-zinc spinel nanocrystals obtained by impregnation with an aqueous solution ($Co_{2.6}Zn_{0.4}O_4|Al_2O_3$), the faceting of the retrieved morphologies is shifted towards enhanced exposure of the (111) plane. The morphology of $Co_3O_4|Al_2O_3$, in turn, is characterized by a more balanced abundance of the low index (100), (110) and (111) facets (Fig. 5 d_1-d_5). The STEM/HAADF investigations and image analysis of the spinel nanocrystals shapes lead to the

conclusion that by using glycerol-assisted or glycerol-free synthesis or by zinc doping of the spinel host the shape of the supported cobalt spinel nanocrystals can be modified in a rather wide range of abundance of the low index (100), (110) and (111) facets, while preserving the overall polyhedral characteristics in all the samples. This allows for the application of such catalysts for resolving the shape-reactivity relationships in a more controlled fashion in comparison to previous studies, where various catalysts of entirely unlike origin were used. It is also worth noting that the applied cobalt spinel nanocrystal shape analysis has been successfully used in accounting for structure sensitivity of N_2O decomposition,[47] methane combustion[55] and $^{16}O^{18}O$ isotopic exchange.[56]

In order to examine the surface composition of the catalysts (Co/Al and Co^{3+}/Co^{2+} ratios) the XPS spectra shown in Fig. 6 were analyzed. The representative survey scan (Fig. 6a) confirms the presence of constituting elements on the catalysts and the absence of surface contamination by spurious elements. The diagnostic scan for Co 2p region, shown in Fig. 6 b_1-e_1, (b-$Co_{2.6}Zn_{0.4}O_4|Al_2O_3$-gly c-$Co_3O_4|Al_2O_3$-gly d-$Co_{2.6}Zn_{0.4}O_4|Al_2O_3$, e-$Co_3O_4|Al_2O_3$) consists of several overlapping features originating from the $2p_{3/2}$ and $2p_{1/2}$ peaks due to Co^{3+} (778.6 ± 0.3 and 793.7 ± 0.4 eV) and Co^{2+} (780.0 ± 0.4 and 795.5 ± 0.2 eV), together with the associated satellite structures in a range of 783.8–788.4 and 803.2 eV, (Table 2)[57]. Additionally, the O 1s and Al 2p regions for all samples are presented in Fig. 6 b_2-e_2 and b_3-e_3, respectively. The derived Co/Al ratio values collected in Table 3 are fairly constant (0.16 - 0.19) and their small deviations result from the varying cobalt loading as determined from XRF measurements (0.06 - 0.08). The higher XPS values are in line with the surface location of cobalt, expected for the supported catalyst. It may be thus concluded that all the obtained catalysts exhibit a similar number of the exposed cobalt active sites, within the experimental error. Nonetheless, for sensible comparison of the catalytic performance of the investigated samples, the determined Co/Al ratio was used for normalization

of the catalytic performance, which is commonly applied for the evaluation of the supported catalyst activity.

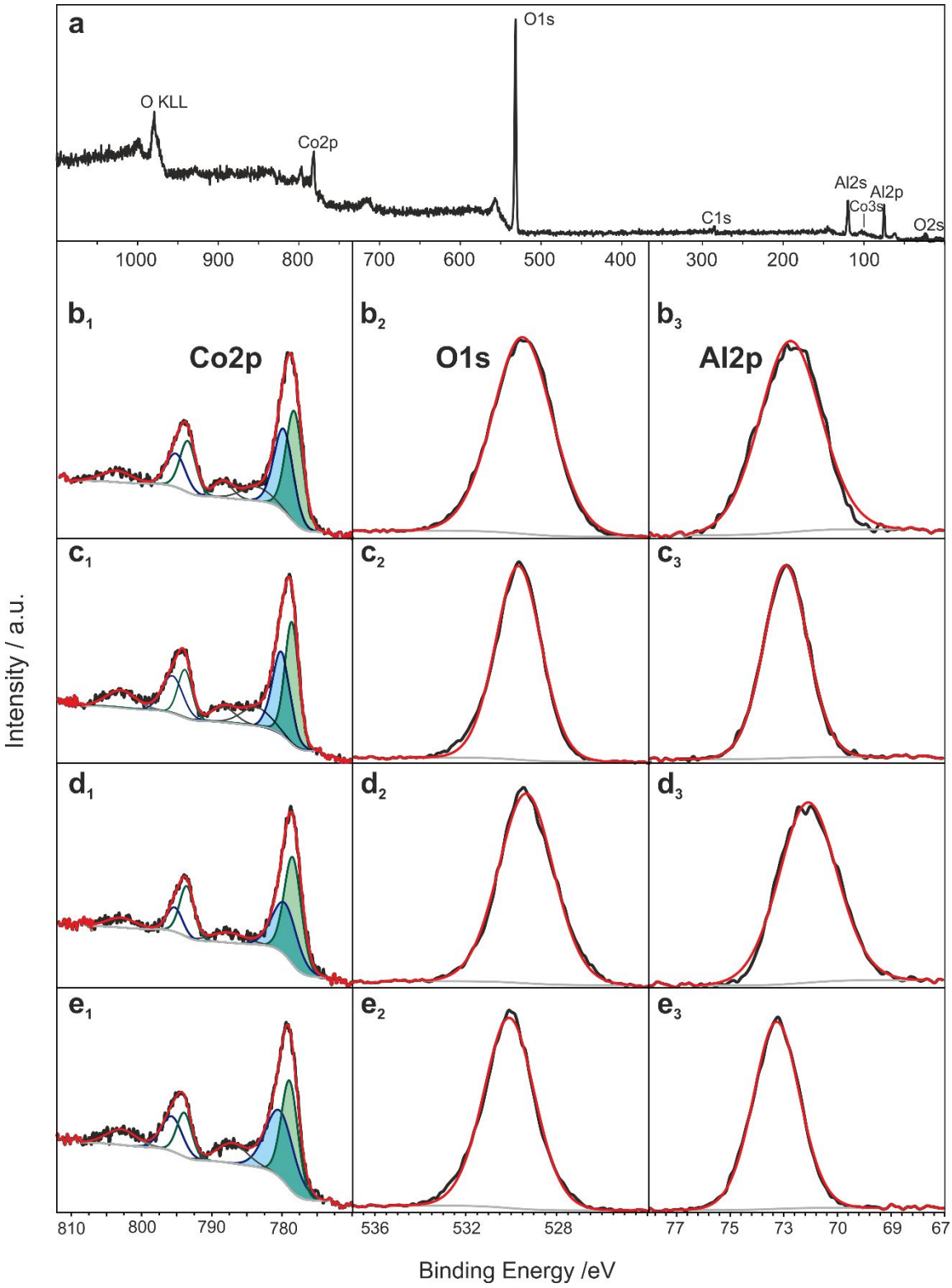

Figure 6. The representative survey scan (a) together with the diagnostic scans for Co 2p, O 1s and Al 2p regions for (b) $Co_{2.6}Zn_{0.4}O_4|Al_2O_3$-gly, (c) $Co_3O_4|Al_2O_3$-gly, (d) $Co_{2.6}Zn_{0.4}O_4|Al_2O_3$ and (e) $Co_3O_4|Al_2O_3$ samples.

Table 2. Co 2p binding energies with the corresponding assignments.

Co 2p, binding Energy/eV				
$Zn_{0.4}Co_{2.6}O_4|Al_2O_3$-gly	$Co_3O_4|Al_2O_3$-gly	$Zn_{0.4}Co_{2.6}O_4|Al_2O_3$	$Co_3O_4|Al_2O_3$	Assign.
778.3	778.7	778.4	778.9	Co^{3+}
779.8	780.3	779.6	780.3	Co^{2+}
783.8	783.8	787.6	787.1	Satellite
788.4	788.4	-	-	
793.4	793.9	793.5	793.9	Co^{3+}
795.2	795.7	795.3	795.7	Co^{2+}
803.6	803.0	803.0	803.0	satelitte

In order to determine the Co^{3+}/Co^{2+} ratio from the XPS data the deconvolution of the Co $2p_{3/2}$ line into the Co^{3+} and Co^{2+} components was performed. The results are collected in Table 3.

It should be emphasized, however, that the determined values are biased by the contribution from the subsurface layers (with the constant bulk ratio regardless the exposed plane), so they do not reflect variations of the actual outermost surface Co^{3+}/Co^{2+} composition exactly. This point will be further elucidated along with the TEM data analysis.

Table 3. Comparison of Co/Al, Zn/Co and Co^{3+}/Co^{2+} atomic ratios determined by different techniques.

Catalyst	Co/Al		Zn/Co	Co^{3+}/Co^{2+}	
	XPS	XRF	XRF	XPS	TEM
$Zn_{0.4}Co_{2.6}O_4|Al_2O_3$-gly	0.19	0.08	0.13	1.7	2.70
$Co_3O_4|Al_2O_3$-gly	0.17	0.07	-	1.4	2.45
$Zn_{0.4}Co_{2.6}O_4|Al_2O_3$	0.15	0.06	0.13	1.4	1.56
$Co_3O_4|Al_2O_3$	0.16	0.06	-	0.9	1.44

3.2 Catalytic performance

The impact of the catalyst morphology on the catalytic performance was probed by the CO-PROX reaction. Figure 7a shows the CO conversion profiles as a function of temperature for the investigated samples. The positive effect of the glycerol-assisted synthesis on the catalytic performance is clearly demonstrated, as the catalyst activity window is shifted toward lower temperature by 40ºC with respect to the samples prepared by glycerol-free route. Furthermore, the Zn-doping of the cobalt spinel enhances the conversion when compared to the bare cobalt spinel.

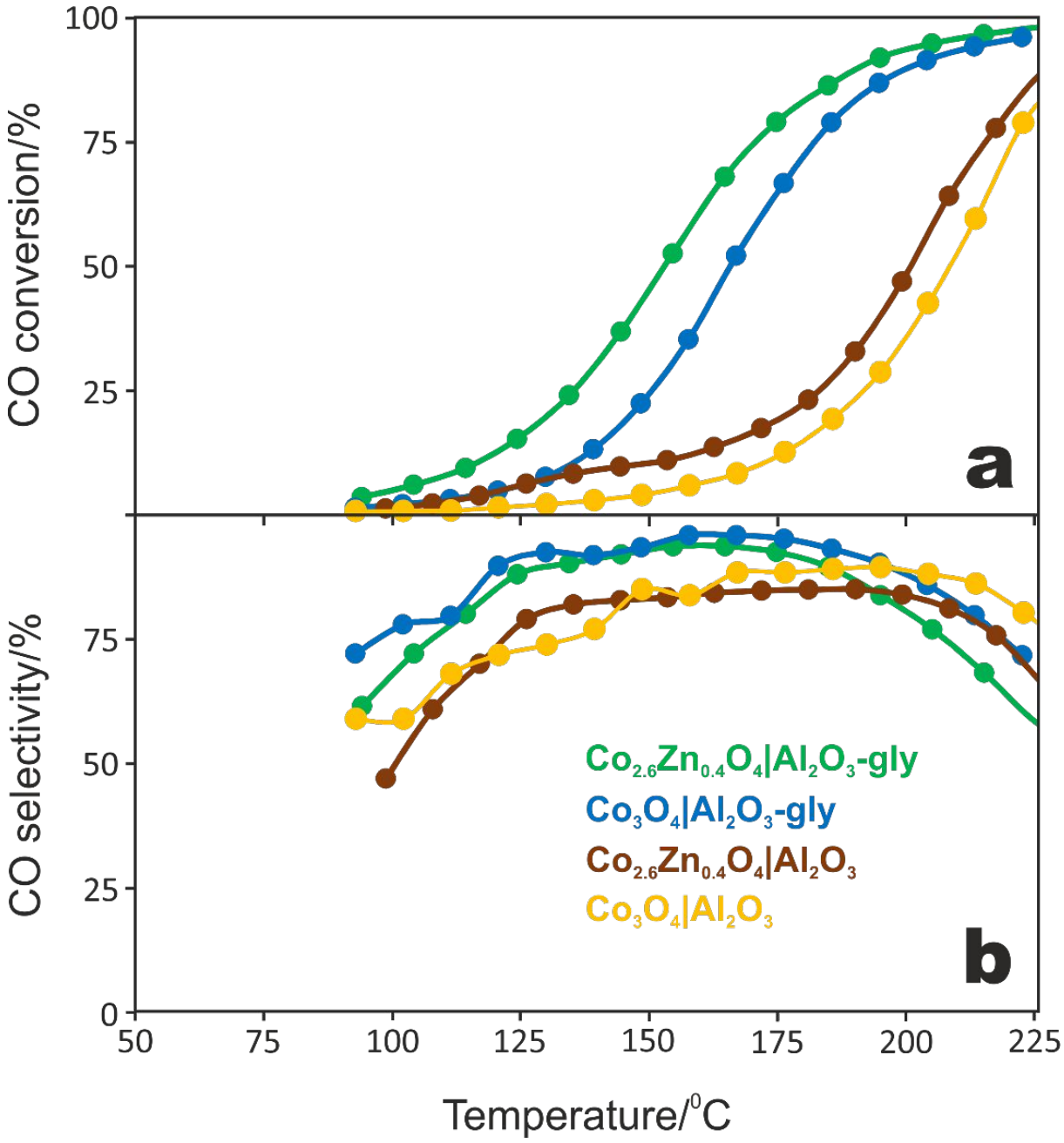

Figure 7. Supported cobalt spinel catalyst performance in the CO-PROX reaction: (a) CO conversion and (b) CO selectivity profiles.

Yet, this effect is much less pronounced in contrast to the superior catalytic behavior of the samples synthesized with the glycerol addition. Upon zinc doping, the conversion curves are shifted to the lower temperature by 10ºC only. The CO selectivity (Fig. 7b) is also higher for the samples prepared with glycerol for the reaction temperatures of practical interest (< 200ºC). The effect of the zinc doping on the CO oxidation selectivity below 180 - 190ºC is essentially negligible, but above this temperature threshold, it becomes distinctly negative. Summarizing, like in the case of other catalysts based on transition metal oxides, such as CuO/ceria or CuO/$KMnO_x$,[58,59] the observed selectivity of the alumina supported spinel catalysts is at a comparable high level (~90%), fulfilling the demanding CO-PROX requirements.

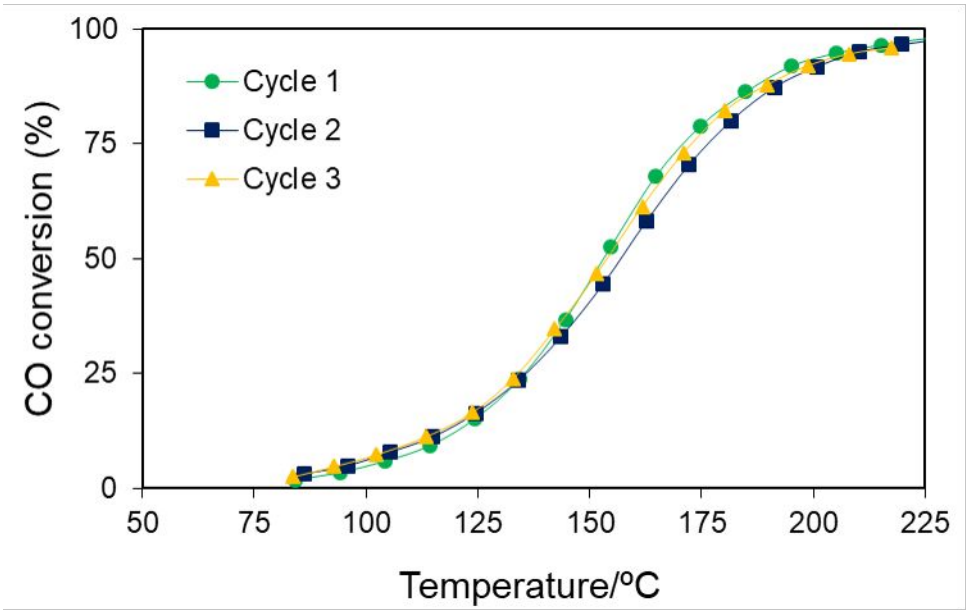

Fig. 8 The reproducibility of CO conversion measurements within the 3 reaction cycles conducted on the $Co_{2.6}Zn_{0.4}O_4|Al_2O_3$-gly catalyst.

As shown in Fig. 8 for the representative example of the $Co_{2.6}Zn_{0.4}O_4|Al_2O_3$-gly sample, along 3 cycles with switching to oxidant atmosphere in between (during cooling down of the reactor), the catalysts showed practically the same behavior (the average error of the catalytic data reproducibility is below 4%).

3.3 Influence of the catalysts morphology on PROX performance

As discussed above, the investigated cobalt spinels supported on alumina differ significantly in their shape, and hence in the number and nature of the exposed cobalt active sites (Co^{3+} vs. Co^{2+}). Therefore, the observed CO-PROX performance was examined with respect to the relative abundance of the (100), (110) and (111) facets exposed by the polyhedral spinel nanograins of the catalysts. The atomic structure of the most stable (100), (110) and (111) terminations is presented in the Supporting Information S5. The following types of cobalt cations are exposed at the spinel surface: i) protruding trivalent cobalt cations located in the octahedral interstitials $(Co_{nc}^{O})^{3+}$ with the coordination number *nc* = 3, 4 or 5 for the (100), (110) and (111) facet, respectively; ii) protruding divalent cobalt cations located in the tetrahedral sites $(Co_{nc}^{T})^{2+}$ with the coordination number equal to 2 for the (100) facet and 3 for the (110) and (111) facets. The stable (100) termination exhibits the following cationic composition: $\{4Co^{O}_{5c}, 1Co^{T}_{2c}, 2Co^{T}_{4c}\}$. The surface concentration of the $(Co^{O}_{5c})^{3+}$ ions is equal to 0.06 ion $Å^{-2}$, whereas the concentration of the $(Co^{T}_{2c})^{2+}$ ions equals 0.015 ion $Å^{-2}$ is four times lower.[45] The cationic composition of the (110) facet is balanced $\{4Co^{O}_{4c}, 4Co^{T}_{3c}\}$, and the areal concentration of both centers is equal to 0.04 ion $Å^{-2}$.[60] In contrast to previous planes, the (111) termination is dominated by the divalent cobalt $\{2Co^{O}_{3c}, 4Co^{T}_{3c}\}$, with the corresponding concentration of the $(Co^{O}_{3c})^{3+}$ = 0.02 ion $Å^{-2}$ and $(Co^{T}_{3c})^{2+}$ = 0.04 ion $Å^{-2}$ surface cations.[60]

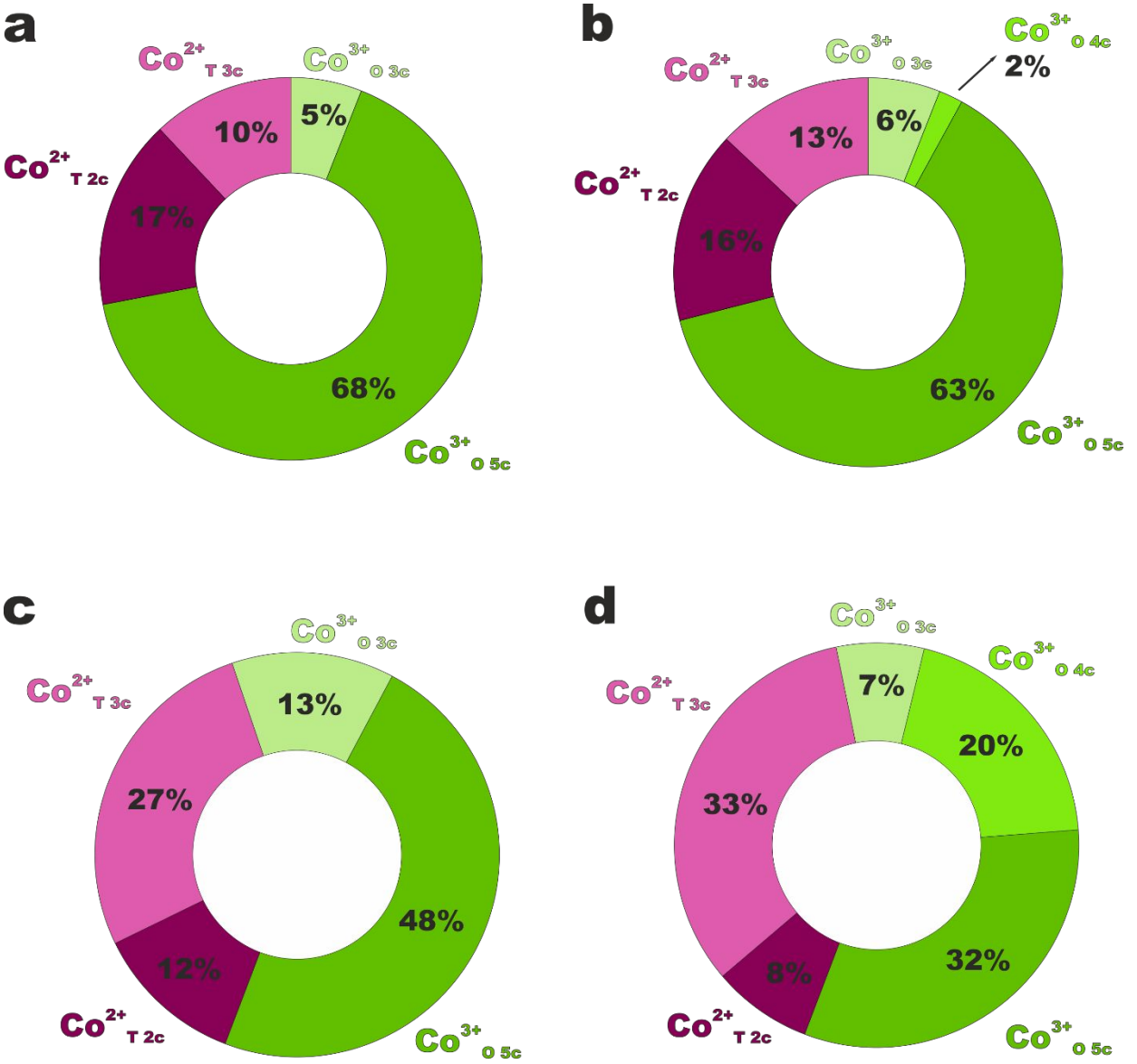

Figure 9. Circle diagrams of percentage composition of accessible octahedral and tetrahedral cationic sites located on facets of cobalt spinel nanocrystals, synthesized with and without glycerol medium a) $Co_{2.6}Zn_{0.4}O_4|Al_2O_3$-gly b) $Co_3O_4|Al_2O_3$-gly c) $Co_{2.6}Zn_{0.4}O_4|Al_2O_3$ and d) $Co_3O_4|Al_2O_3$.

Upon combining the cationic composition of the exposed planes with the average relative contribution of each facet to the overall morphology of the spinel polyhedral nanocrystals (Fig. 5), it was possible to assess the mean fraction of the particular $(Co_{nc}^{O})^{3+}$ or $(Co_{nc}^{T})^{2+}$ active sites, exposed by the spinel active phase for all the investigated samples (Supporting information, Table S1).

In Figure 9 the percentage content of the nominally accessible Co^{3+} (marked in green) and Co^{2+} (purple) active sites is presented in the form of circular diagrams with the estimated relative error of 10%. In order to clarify the effect of the cobalt spinel faceting on the CO conversion in CO-PROX reaction, the values of the apparent reaction rate (r_{CO}) in the temperature range of 150 – 200°C were correlated with the relative abundance of the particular low index (100), (111) and (110) facets for all the examined catalysts. The results presented in Figure 10a reveal that the apparent rate of the PROX reaction over the supported spinel catalysts is clearly well-correlated with the surface abundance of the (100) facet, for all the investigated temperatures.

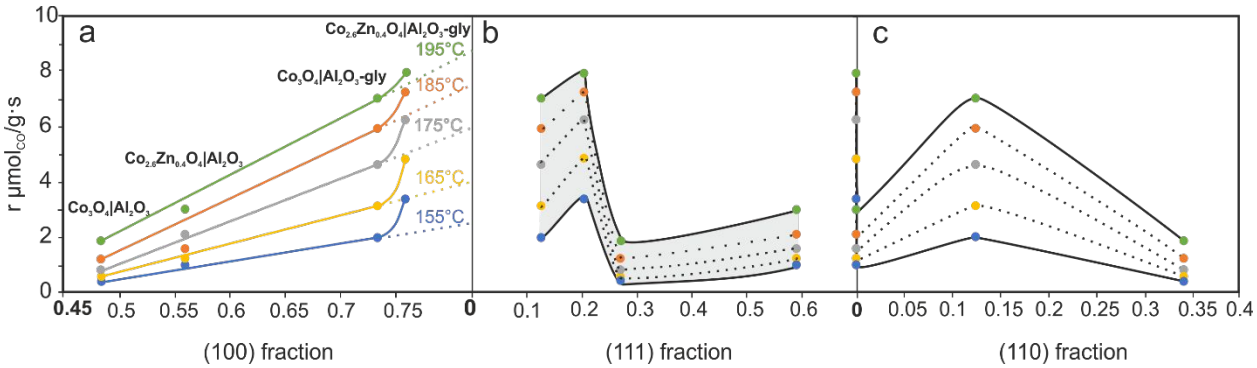

Figure 10. The apparent reaction rate (r_{CO}) versus the relative abundance of a) (100), b) (111) and c) (110) facet for $Co_3O_4|Al_2O_3$, $Co_{2.6}Zn_{0.4}O_4|Al_2O_3$, $Co_3O_4|Al_2O_3$-gly and

$Co_{2.6}Zn_{0.4}O_4|Al_2O_3$-gly catalysts in CO-PROX reaction at the temperature range of 150 - 200°C.

This fact stays in an evident variance with the apparent lack of such correlation between the fraction of the (111) and (110) facets and the CO-PROX rate (Fig. 10b,c). A distinct deviation from the linearity, observed in the case of the $Co_{2.6}Zn_{0.4}O_4|Al_2O_3$-gly sample (Fig. 10a), is attributed to a beneficial effect of Zn cations located in tetrahedral interstitials for activation of the dioxygen reactant. Indeed, our previous investigations have shown that zinc cations lower the catalyst work function,[61] favoring O_2 activation via interfacial electron transfer.[47] However, it should be noted that such an increase in the catalyst activity is associated with an appreciable drop of the CO oxidation selectivity (Fig. 7b). For a lower abundance of the (100) plane the Zn effect is probably too low to be manifested and more systematic studies with variable zinc content are required to resolve this problem sensibly.

The obtained results indicate a strong impact of the morphological factor, associated with the exposition of the beneficial (100) facet, on the catalytic performance of the investigated samples in CO-PROX reaction. It can be explained by the fact that the (100) facets exhibit the highest surface concentration of the Co^{3+} cations, which, contrary to Co^{2+}, are believed to act as PROX active sites. In line with this conjecture, we analyzed the effect of the total abundance of surface Co^{3+} determined from TEM analysis on the CO-PROX reaction yield, normalized to the Co/Al ratio in the temperature range of 150 – 200°C. The results presented in Figure 11 show clearly that the reaction yield rises linearly with the amount of the exposed Co^{3+} cations, providing for the first time quantitative arguments in favor of their decisive role in the catalytic PROX turn-over. The same trend was observed for the dependence of the normalized yield as a function of the Co^{3+}/Co^{2+}

ratio obtained from the XPS data. However, as already argued, in the latter case the determined ratio is buffered by the subsurface contribution, therefore, the observed dependence, though noticeable, is apparently attenuated (see Fig. S6). This observation may be traced back to the reported higher affinity of Co^{3+} species toward CO capture when compared to Co^{2+}.[62] The Co^{2+} cations, in turn, are believed to favor H_2 dissociation,[63] triggering a competitive process that can take place in parallel to the preferred CO oxidation reaction. As the described method of glycerol-assisted synthesis of the cobalt spinel/alumina catalyst is easily scalable,[29,30] the obtained results have also practical importance for manufacturing of the real CO-PROX catalyst with an enhanced abundance of the most active (100) Co_3O_4 plane.

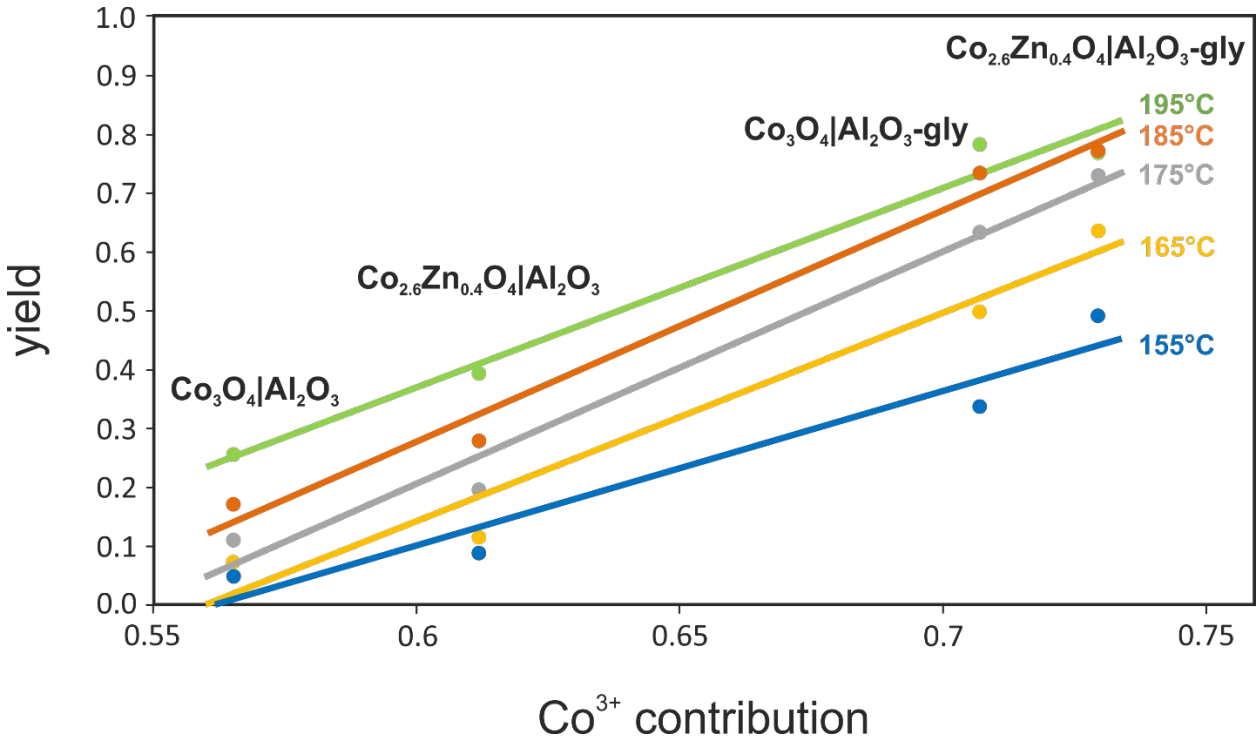

Figure 11. The reaction yield versus a) (100), b) (111) and c) (110) facets abundance for $Co_3O_4|Al_2O_3$, $Co_{2.6}Zn_{0.4}O_4|Al_2O_3$, $Co_3O_4|Al_2O_3$-gly and $Co_{2.6}Zn_{0.4}O_4|Al_2O_3$-gly catalysts in CO-PROX reaction for the temperature range of 150 - 200°C.

Since, the morphology of $Co_{2.6}Zn_{0.4}O_4|Al_2O_3$-gly, $Co_3O_4|Al_2O_3$-gly, $Co_{2.6}Zn_{0.4}O_4|Al_2O_3$, and $Co_3O_4|Al_2O_3$ nanocrystals, is predominated by the (100) and (111) facets, their stabilities in the bare, oxygen, water, CO covered and oxygen vacancy defected states were analyzed within the CO- PROX reaction conditions: 0^0C – 300^0C and $p_{O_2}/p_0 = 10^{-4}$ (Figure 12 a, b, green region).

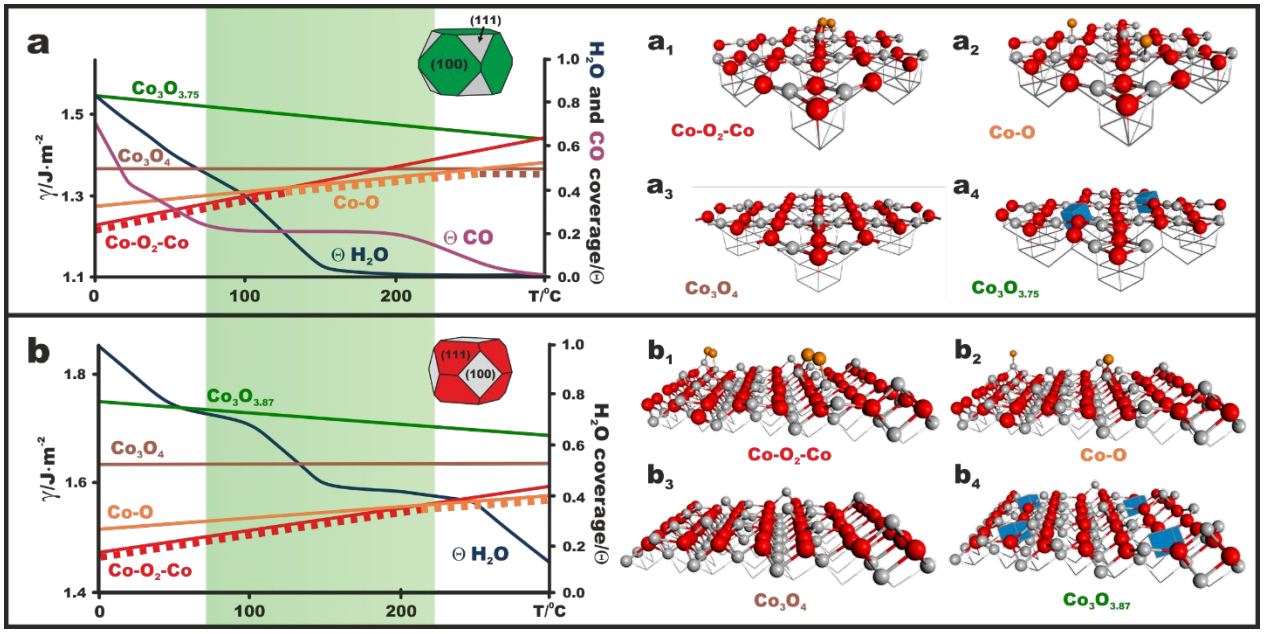

Figure 12. *left*: Surface energies (γ/J•m^{-2}) of a) (100) (green) and b) (111) (red) terminations, bare (brown line) and covered with reactive oxygen species (ROS) (red and

orange line), together with water coverage, Θ (blue line), and carbon oxide (violet line) coverage, Θ plotted against temperature, for the temperature range 0°C – 300°C and $p_{O_2}/p_0 = 10^{-4}$, covering the CO-PROX reaction conditions (green region). ***right***: Atomic structures of selected terminations of $a_1 – a_4$) (100) and $b_1 – b_4$) (111) facets. Color coding: ROS - orange spheres, anions crystal sublattice - red spheres, metal cations crystal sublattice – grey spheres, oxygen vacancies – blue cubes.

This Figure was constructed using the surface energies calculated by us previously[45,46] for analyzing the catalytic behavior of cobalt spinel in deN_2O and CH_4 oxidation reactions. As can be inferred from Fig. 12ab both (100) and (111) facets are covered by diatomic (Co-O_2-Co) or monoatomic (Co-O) reactive oxygen species (*cf.* red and orange lines Figure 12 a, b) in the whole range of the PROX reaction. The structures of the ROS covered (100) and (111) surfaces are presented in Figure 12 a_1, a_2, and b_1, b_2, respectively. The bare stoichiometric (100) and (111) surfaces and their defected states by the formation of oxygen vacancies are situated much higher in energy (Figure 12 a_3, b_3,), so their abundance in the CO-PROX conditions is negligible. The structure of both

terminations with the oxygen vacancies represented as blue cubes, are presented in Figure 12, a_4, b_4. These results imply that in CO-PROX reaction conditions the spinel surface is covered by reactive oxygen species, which are engaged in CO oxidation.[47,48] The alternative mechanism involving formation and refilling of oxygen surface vacancies is precluded because of the high energy cost of their formation (see green line in Fig. 12). Analysis of the temperature dependence of the cobalt spinel surface water coverage provides another argument speaking in favor of superior behavior of the (100) facet over the (111). Water is formed as a product of the competing, undesired side reaction of hydrogen combustion. The produced H_2O molecules can block the active sites of the spinel nanocrystals. Figure 12 a, b shows changes in the water coverage of both terminations as a function of the CO-PROX reaction progress with temperature. In the case of the (100) termination water coverage changes from 0.45 at the reaction onset till nearly zero above ~150°C. For (111) termination the water retention is much higher, changing from 0.75 to 0.4. As a result, such surface is blocked to a large extent by the side reaction product slowing down the target CO oxidation pathway. As it can be seen in Figure 12a, at low temperatures there is a coexistence of CO, H_2O and ROS forms on the (100) surface. For the temperatures higher than 130°C, water coverage is highly reduced (Θ_{H2O}, blue line in Fig 12a), and the free cobalt active sites are accessible for CO adsorption (violet line). This temperature range corresponds to high

activity of the (100) facet, whereas the low temperature range is disguised by the active site blocking effect due to water retention on the surface.

Summarizing, the performed thermodynamic analysis in the CO-PROX conditions implies that the reaction occurs preferentially on the (100) plane of the cobalt spinel surface via suprafacial oxidation mechanisms. Additionally, such termination is the most resistant to self-poisoning by water, and involvement of the alternative Mars-van Krevelen mechanism is unlikely due to the high energetic cost of the oxygen vacancies formation.

CONCLUSIONS

Alumina-supported Co_3O_4 catalysts with variable abundance of the (100), (111) and (110) facets were synthesized by glycerol and/or by Zn addition to the impregnation solution, while preserving the overall polyhedral shape of the nano-spinel active phase. The morphology of the cobalt spinel nanoparticles strongly influences the CO conversion in CO-PROX reaction of the obtained catalysts. The (100) termination was found to be the most active among the all exposed low index planes ((100), (111) and (110)). A linear correlation between the content of the surface Co^{3+} cations and the CO oxidation yield confirms experimentally their key role as the reaction active sites. The constructed thermodynamic diagram provides a rational background for the advantage of the (100) termination in the CO-PROX reaction and the involvement of the suprafacial oxygen species in the CO oxidation step.

SUPPORTING INFORMATION

The percentage composition of accessible octahedral and tetrahedral cationic sites located on the (100), (110) and (111) facets of spinel nanocrystals of investigated catalysts, the shape analysis of the observed nanocrystals by adjusting properly oriented Wulff hulls to the experimental edge patterns and the reaction yield normalized to Co/Al ratio (determined from XPS) versus Co^{3+} contribution determined by XPS.

AUTHOR INFORMATION

Corresponding Author

*Gabriela Grzybek; email: g.grzybek@uj.edu.pl

AUTHOR CONTRIBUTIONS

The manuscript was written through contributions of all authors. All authors have given approval to the final version of the manuscript.

ACKNOWLEDGMENT

Authors would like to acknowledge the funding awarded by the Polish National Science Center (decision number 2017/27/B/ST4/01155), the financial support from Generalitat

Valenciana (Project PROMETEOII/2014/010), Spanish Ministry of Economy and Competitiveness (Project CTQ2015-67597-C2-2-R), Spanish Ministry of Education, Culture and Sports (grant FPU14/01178).

The research was partially carried out with the equipment purchased thanks to the financial support of the European Regional Development Fund in the framework of the Polish Innovation Economy Operational Program (contract no. POIG.02.01.00-12-023/08).

REFERENCES

(1) Choudhary, T. .; Goodman, D. CO-Free Fuel Processing for Fuel Cell Applications. *Catal. Today* **2002**, *77* (1–2), 65–78. https://doi.org/10.1016/S0920-5861(02)00233-X.

(2) Park, E. D.; Lee, D.; Lee, H. C. Recent Progress in Selective CO Removal in a H_2-Rich Stream. *Catal. Today* **2009**, *139* (4), 280–290. https://doi.org/10.1016/J.CATTOD.2008.06.027.

(3) Yao, S.; Mudiyanselage, K.; Xu, W.; Johnston-Peck, A. C.; Hanson, J. C.; Wu, T.; Stacchiola, D.; Rodriguez, J. A.; Zhao, H.; Beyer, K. A.; et al. Unraveling the Dynamic Nature of a CuO/CeO_2 Catalyst for CO Oxidation in *Operando*: A Combined Study of XANES (Fluorescence) and DRIFTS. *ACS Catal.* **2014**, *4* (6), 1650–1661. https://doi.org/10.1021/cs500148e.

(4) Wang, W.-W.; Yu, W.-Z.; Du, P.-P.; Xu, H.; Jin, Z.; Si, R.; Ma, C.; Shi, S.; et. al.Crystal Plane Effect of Ceria on Supported Copper Oxide Cluster Catalyst for CO Oxidation: Importance of Metal–Support Interaction. *ACS Catal.* **2017**, *7* (2), 1313–1329. https://doi.org/10.1021/acscatal.6b03234.

(5) Martínez-Arias, A.; Gamarra, D.; Hungría, A.; Fernández-García, M.; Munuera, G.; Hornés, A.; Bera, P.; Conesa, J.; Cámara, A. Characterization of Active Sites/Entities and Redox/Catalytic Correlations in Copper-Ceria-Based Catalysts for Preferential Oxidation of CO in H_2-Rich Streams. *Catalysts* **2013**, *3* (2), 378–400. https://doi.org/10.3390/catal3020378.

(6) Polster, C. S.; Nair, H.; Baertsch, C. D. Study of Active Sites and Mechanism Responsible for Highly Selective CO Oxidation in H_2 Rich Atmospheres on a Mixed Cu and Ce Oxide Catalyst. *J. Catal.* **2009**, *266* (2), 308–319. https://doi.org/10.1016/J.JCAT.2009.06.021.

(7) Elias, J. S.; Stoerzinger, K. A.; Hong, W. T.; Risch, M.; Giordano, L.; Mansour, A. N.; Shao-Horn, Y. In Situ Spectroscopy and Mechanistic Insights into CO Oxidation on Transition-Metal-Substituted Ceria Nanoparticles. *ACS Catal.* **2017**, *7* (10), 6843–6857. https://doi.org/10.1021/acscatal.7b01600.

(8) Manasilp, A.; Gulari, E. Selective CO Oxidation over Pt/Alumina Catalysts for Fuel Cell Applications. *Appl. Catal. B Environ.* **2002**, *37* (1), 17–25. https://doi.org/10.1016/S0926-3373(01)00319-8.

(9) Kahlich, M. J.; Gasteiger, H. A.; Behm, R. J. Kinetics of the Selective CO Oxidation in H_2-Rich Gas on Pt/Al2O3. *J. Catal.* **1997**, *171* (1), 93–105. https://doi.org/10.1006/JCAT.1997.1781.

(10) Wootsch, A.; Descorme, C.; Duprez, D. Preferential Oxidation of Carbon Monoxide in the Presence of Hydrogen (PROX) over Ceria–Zirconia and Alumina-Supported Pt Catalysts. *J. Catal.* **2004**, *225* (2), 259–266. https://doi.org/10.1016/J.JCAT.2004.04.017.

(11) Navlani-García, M.; Martis, M.; Lozano-Castelló, D.; Cazorla-Amorós, D.; Mori, K.; Yamashita, H. Investigation of Pd Nanoparticles Supported on Zeolites for Hydrogen Production from Formic Acid Dehydrogenation. *Catal. Sci. Technol.* **2015**, *5* (1), 364–371. https://doi.org/10.1039/C4CY00667D.

(12) Han, Y.-F.; Kahlich, M. J.; Kinne, M.; Behm, R. J. Kinetic Study of Selective CO Oxidation in H_2-Rich Gas on a Ru/γ-Al_2O_3 Catalyst. *Phys. Chem. Chem. Phys.* **2002**, *4* (2), 389–397. https://doi.org/10.1039/b103780n.

(13) Grisel, R. J.; Weststrate, C.; Goossens, A.; Crajé, M. W.; van der Kraan, A.; Nieuwenhuys, B. Oxidation of CO over Au/MO_x/Al_2O_3 Multi-Component Catalysts in a Hydrogen-Rich Environment. *Catal. Today* **2002**, *72* (1–2), 123–132. https://doi.org/10.1016/S0920-5861(01)00486-2.

(14) Schubert, M. M.; Hackenberg, S.; van Veen, A. C.; Muhler, M.; Plzak, V.; Behm, R. J. CO Oxidation over Supported Gold Catalysts—"Inert" and "Active" Support Materials and Their Role for the Oxygen Supply during Reaction. *J. Catal.* **2001**, *197* (1), 113–122. https://doi.org/10.1006/JCAT.2000.3069.

(15) Bethke, G.; Kung, H.Selective CO Oxidation in a Hydrogen-Rich Stream over Au/γ-Al_2O_3 Catalysts. *Appl. Catal. A Gen.* **2000**, *194–195*, 43–53. https://doi.org/10.1016/S0926-860X(99)00352-X.

(16) Mariño, F.; Descorme, C.; Duprez, D. Supported Base Metal Catalysts for the Preferential Oxidation of Carbon Monoxide in the Presence of Excess Hydrogen (PROX). *Appl. Catal. B Environ.* **2005**, *58* (3–4), 175–183. https://doi.org/10.1016/J.APCATB.2004.12.008.

(17) Huang, T.-J.; Yu, T.-C. Calcination Conditions on Copper/Alumina Catalysts for Carbon Monoxide Oxidation and Nitric Oxide Reduction. *Appl. Catal.* **1991**, *71* (2), 275–282. https://doi.org/10.1016/0166-9834(91)85085-A.

(18) Zhang, S.-M.; Huang, W.-P.; Qiu, X.-H.; Li, B.-Q.; Zheng, X.-C.; Wu, S.-H. Comparative Study on Catalytic Properties for Low-Temperature CO Oxidation of Cu/CeO_2 and CuO/CeO_2 Prepared via Solvated Metal Atom Impregnation and Conventional Impregnation. *Catal. Letters* **2002**, *80* (1/2), 41–46. https://doi.org/10.1023/A:1015318525080.

(19) Luo, J.-Y.; Meng, M.; Zha, Y.-Q.; Guo, L.-H. Identification of the Active Sites for CO and C_3H_8 Total Oxidation over Nanostructured CuO−CeO_2 and Co_3O_4−CeO_2 Catalysts. *J. Phys. Chem. C* **2008**, *112* (23), 8694–8701. https://doi.org/10.1021/jp800651k.

(20) Luo, J.-Y.; Meng, M.; Li, X.; Li, X.-G.; Zha, Y.-Q.; Hu, T.-D.; Xie, Y.-N.; Zhang, J. Mesoporous Co_3O_4–CeO_2 and Pd/Co_3O_4–CeO_2 Catalysts: Synthesis, Characterization and

Mechanistic Study of Their Catalytic Properties for Low-Temperature CO Oxidation. *J. Catal.* **2008**, *254* (2), 310–324. https://doi.org/10.1016/J.JCAT.2008.01.007.

(21) Yang, J.; Guo, J.; Wang, Y.; Wang, T.; Gu, J.; Peng, L.; Xue, N.; Zhu, Y.; Guo, X.; Ding, W. Reduction-Oxidation Pretreatment Enhanced Catalytic Performance of Co_3O_4/Al_2O_3 over CO Oxidation. *Appl. Surf. Sci.* **2018**, *453*, 330–335. https://doi.org/10.1016/J.APSUSC.2018.05.103.

(22) Caputo, T.; Lisi, L.; Pirone, R.; Russo, G. On the Role of Redox Properties of CuO/CeO_2 Catalysts in the Preferential Oxidation of CO in H_2-Rich Gases. *Appl. Catal. A Gen.* **2008**, *348* (1), 42–53. https://doi.org/10.1016/J.APCATA.2008.06.025.

(23) Avgouropoulos, G.; Ioannides, T.; Matralis, H. K.; Batista, J.; Hocevar, S. $CuO–CeO_2$ Mixed Oxide Catalysts for the Selective Oxidation of Carbon Monoxide in Excess Hydrogen. *Catal. Letters* **2001**, *73* (1), 33–40. https://doi.org/10.1023/A:1009013029842.

(24) Martínez-Arias, A.; Fernández-García, M.; Soria, J.; Conesa, J. C. Spectroscopic Study of a Cu/CeO_2 Catalyst Subjected to Redox Treatments in Carbon Monoxide and Oxygen. *J. Catal.* **1999**, *182* (2), 367–377. https://doi.org/10.1006/JCAT.1998.2361.

(25) Bion, N.; Epron, F.; Moreno, M.; Mariño, F.; Duprez, D. Preferential Oxidation of Carbon Monoxide in the Presence of Hydrogen (PROX) over Noble Metals and Transition Metal Oxides: Advantages and Drawbacks. *Top. Catal.* **2008**, *51* (1–4), 76–88. https://doi.org/10.1007/s11244-008-9116-x.

(26) Guo, Q.; Liu, Y. MnOx Modified Co_3O_4-CeO_2 Catalysts for the Preferential Oxidation of CO in H_2-Rich Gases. *Appl. Catal. B Environ.* **2008**, *82* (1–2), 19–26. https://doi.org/10.1016/J.APCATB.2008.01.007.

(27) Woods, M. P.; Gawade, P.; Tan, B.; Ozkan, U. S. Preferential Oxidation of Carbon Monoxide on Co/CeO_2nanoparticles. *Appl. Catal. B Environ.* **2010**, *97* (1–2), 28–35. https://doi.org/10.1016/j.apcatb.2010.03.015.

(28) Zhao, Z.; Yung, M. M.; Ozkan, U. S. Effect of Support on the Preferential Oxidation of CO over Cobalt Catalysts. *Catal. Commun.* **2008**, *9* (6), 1465–1471. https://doi.org/10.1016/J.CATCOM.2007.12.013.

(29) Grzybek, G.; Wójcik, S.; Ciura, K.; Grybo, J.; Indyka, P.; Oszajca, M.; Stelmachowski, P.; Witkowski, S.; Inger, M.; Wilk, M.; et al. Influence of Preparation Method on Dispersion of Cobalt Spinel over Alumina Extrudates and the Catalyst DeN_2O Activity. *Appl. Catal. B Environ.* **2017**, *210*, 34–44. https://doi.org/10.1016/j.apcatb.2017.03.053.

(30) Gudyka, S.; Grzybek, G.; Gryboś, J.; Indyka, P.; Leszczyński, B.; Kotarba, A.; Sojka, Z. Enhancing the DeN_2O Activity of the Supported $Co_3O_4|\alpha$-Al_2O_3 Catalyst by Glycerol-Assisted Shape Engineering of the Active Phase at the Nanoscale. *Appl. Catal. B Environ.* **2017**, *201*, 339–347. https://doi.org/10.1016/J.APCATB.2016.08.034.

(31) Hu, L.; Peng, Q.; Li, Y. Selective Synthesis of Co_3O_4 Nanocrystal with Different Shape and Crystal Plane Effect on Catalytic Property for Methane Combustion . *Am. Chem. Soc.***2008**, 130, (48), 16136-16137. https://doi.org/10.1021/ja806400e.

(32) Xie, X.; Li, Y.; Liu, Z.-Q.; Haruta, M.; Shen, W. Low-Temperature Oxidation of CO Catalysed by Co_3O_4 Nanorods. *Nature* **2009**, *458* (7239), 746–749. https://doi.org/10.1038/nature07877.

(33) Yu, Y.; Takei, T.; Ohashi, H.; He, H.; Zhang, X.; Haruta, M. Pretreatments of Co_3O_4 at Moderate Temperature for CO Oxidation at −80 °C. *J. Catal.* **2009**, *267* (2), 121–128. https://doi.org/10.1016/J.JCAT.2009.08.003.

(34) Khasu, M.; Nyathi, T.; Morgan, D. J.; Hutchings, G. J.; Claeys, M.; Fischer, N. Co_3O_4 Morphology in the Preferential Oxidation of CO. *Catal. Sci. Technol.* **2017**, *7* (20), 4806–

4817. https://doi.org/10.1039/C7CY01194F.
(35) Ciura, K.; Grzybek, G.; Wójcik, S.; Indyka, P.; Kotarba, A.; Sojka, Z. Optimization of Cesium and Potassium Promoter Loading in Alkali-Doped $Zn_{0.4}Co_{2.6}O_4|Al_2O_3$ Catalysts for N_2O Abatement. *React. Kinet. Mech. Catal.* **2017**, *121* (2), 645–655. https://doi.org/10.1007/s11144-017-1188-9.
(36) Inger, M.; Wilk, M.; Saramok, M.; Grzybek, G.; Grodzka, A.; Stelmachowski, P.; Makowski, W.; Kotarba, A.; Sojka, Z. Cobalt Spinel Catalyst for N_2O Abatement in the Pilot Plant Operation–Long-Term Activity and Stability in Tail Gases. *Ind. Eng. Chem. Res.* **2014**, *53* (25), 10335–10342. https://doi.org/10.1021/ie5014579.
(37) Grzybek, G.; Stelmachowski, P.; Gudyka, S.; Indyka, P.; Sojka, Z.; Guillén-Hurtado, N.; Rico-Pérez, V.; Bueno-López, A.; Kotarba, A. Strong Dispersion Effect of Cobalt Spinel Active Phase Spread over Ceria for Catalytic N_2O Decomposition: The Role of the Interface Periphery. *Appl. Catal. B Environ.* **2016**, *180*, 622–629. https://doi.org/10.1016/J.APCATB.2015.07.027.
(38) Grzybek, G.; Wójcik, S.; Legutko, P.; Gryboś, J.; Indyka, P.; Leszczyński, B.; Kotarba, A.; Sojka, Z. Thermal Stability and Repartition of Potassium Promoter between the Support and Active Phase in the $K\text{-}Co_{2.6}Zn_{0.4}O_4|\alpha\text{-}Al_2O_3$ Catalyst for N_2O Decomposition: Crucial Role of Activation Temperature on Catalytic Performance. *Appl. Catal. B Environ.* **2017**, *205*, 597–604. https://doi.org/10.1016/J.APCATB.2017.01.005.
(39) Grzybek, G.; Ciura, K.; Wójcik, S.; Gryboś, J.; Indyka, P.; Inger, M.; Antoniak-Jurak, K.; Kowalik, P.; Kotarba, A.; Sojka, Z. On the Selection of the Best Polymorph of Al_2O_3 Carriers for Supported Cobalt Nano-Spinel Catalysts for N_2O Abatement: An Interplay between Preferable Surface Spreading and Damaging Active Phase–Support Interaction. *Catal. Sci. Technol.* **2017**, *7* (23), 5723–5732. https://doi.org/10.1039/C7CY01575E.
(40) Mitchell, D. R. G.; Schaffer, B. Scripting-Customised Microscopy Tools for Digital Micrograph™. *Ultramicroscopy* **2005**, *103* (4), 319–332. https://doi.org/10.1016/J.ULTRAMIC.2005.02.003.
(41) Canny, J. A. Computational Approach to Edge Detection. *IEEE Trans. Pattern Anal. Mach. Intell.* **1986**, *PAMI-8* (6), 679–698.
(42) E. Meijering, , Biomedical Imaging Group of the Swiss FederalInstitute of Technology in Lausanne (EPFL), S. FeatureJ.
(43) W.S. Rasband, U.S. National Institutes of Health, Bethesda, Maryland, USA, 2014 (1997). ImageJ.
(44) Wulff, G. Zeitschrift Fur Krystallographie Und Mineralogie. **1901**, 449–530.
(45) Zasada, F.; Piskorz, W.; Sojka, Z. Cobalt Spinel at Various Redox Conditions: DFT+U Investigations into the Structure and Surface Thermodynamics of the (100) Facet. *J. Phys. Chem. C* **2015**, *119* (33), 19180–19191. https://doi.org/10.1021/acs.jpcc.5b05136.
(46) Zasada, F.; Gryboś, J.; Piskorz, W.; Sojka, Z. Cobalt Spinel (111) Facets of Various Stoichiometry—DFT+U and *Ab Initio* Thermodynamic Investigations. *J. Phys. Chem. C* **2018**, *122* (5), 2866–2879. https://doi.org/10.1021/acs.jpcc.7b11869.
(47) Zasada, F.; Piskorz, W.; Janas, J.; Gryboś, J.; Indyka, P.; Sojka, Z. Reactive Oxygen Species on the (100) Facet of Cobalt Spinel Nanocatalyst and Their Relevance in $^{16}O_2/^{18}O_2$ Isotopic Exchange, *de* N_2O, and *de*CH_4 Processes—A Theoretical and Experimental Account. *ACS Catal.* **2015**, *5* (11), 6879–6892. https://doi.org/10.1021/acscatal.5b01900.
(48) Zasada; F., Gryboś, J., Budiyanto; E., Janas, J., Sojka, Z. In Press: Oxygen Species Stabilized on the Cobalt Spinel Nano-Octahedra at Various Reaction Conditions and Their Role in Catalytic CO and CH_4 Oxidation, N_2O Decomposition. *ournal Catal.* **2019**, *371*,

24–235.
(49) Zasada, F.; Piskorz, W.; Cristol, S.; Paul, J.-F.; Kotarba, A.; Sojka, Z. Periodic Density Functional Theory and Atomistic Thermodynamic Studies of Cobalt Spinel Nanocrystals in Wet Environment: Molecular Interpretation of Water Adsorption Equilibria. *J. Chem. Phys.* **2010**, *114* (50), 22245–22253. https://doi.org/10.1021/jp109264b.
(50) EUROKIN_fixed-bed_html, EUROKIN spreadsheet on requirements for measurement of intrinsic kinetics in the gas-solid fixed-bed reactor **2012**, www.eurokin.org.
(51) Hadjiev, V. G.; Iliev, M. N.; Vergilov, I. V. The Raman Spectra of Co_3O_4. *J. Phys. C Solid State Phys.* **1988**, *21* (7), L199–L201. https://doi.org/10.1088/0022-3719/21/7/007.
(52) Kaczmarczyk, J.; Zasada, F.; Janas, J.; Indyka, P.; Piskorz, W.; Kotarba, A.; Sojka, Z. Thermodynamic Stability, Redox Properties, and Reactivity of Mn_3O_4, Fe_3O_4, and Co_3O_4 Model Catalysts for N_2O Decomposition: Resolving the Origins of Steady Turnover. *ACS Catal.* **2016**, *6* (2), 1235–1246. https://doi.org/10.1021/acscatal.5b02642.
(53) Lin, H.-K.; Chiu, H.-C.; Tsai, H.-C.; Chien, S.-H.; Wang, C.-B. Synthesis, Characterization and Catalytic Oxidation of Carbon Monoxide over Cobalt Oxide. *Catal. Letters* **2003**, *88* (3/4), 169–174. https://doi.org/10.1023/A:1024013822986.
(54) Kostuch, A.; Gryboś, J.; Indyka, P.; Osmieri, L.; Specchia, S.; Sojka, Z.; Kruczała, K. Morphology and Dispersion of Nanostructured Manganese–Cobalt Spinel on Various Carbon Supports: The Effect on the Oxygen Reduction Reaction in Alkaline Media. *Catal. Sci. Technol.* **2018**, *8* (2), 642–655. https://doi.org/10.1039/C7CY02228J.
(55) Zasada, F.; Janas, J.; Piskorz, W.; Gorczyńska, M. G.; Sojka, Z. Total Oxidation of Lean Methane over Cobalt Spinel Nanocubes Controlled by the Self-Adjusted Redox State of the Catalyst: Experimental and Theoretical Account for Interplay between the Langmuir−Hinshelwood and Mars−Van Krevelen Mechanisms. *ACS Catal.* **2017**, *7*, 2853−2867. https://doi.org/10.1021/acscatal.6b03139.
(56) Zasada, F.; Piskorz, W.; Janas, J.; Budiyanto, E.; Sojka, Z. Dioxygen Activation Pathways over Cobalt Spinel Nanocubes From Molecular Mechanism into Ab Initio Thermodynamics and $^{16}O_2$ /$^{18}O_2$ Exchange Microkinetics. *J. Phys. Chem. C* **2017**, *121* (43), 24128–24143. https://doi.org/10.1021/acs.jpcc.7b09597.
(57) Petitto, S. C.; Marsh, E. M.; Carson, G. A. Cobalt Oxide Surface Chemistry: The Interaction of CoO(1 0 0), Co_3O_4(1 1 0) and Co_3O_4(1 1 1) with Oxygen and Water. *J. Mol. Catal. A Chem.* **2008**, *281* (1–2), 49–58. https://doi.org/10.1016/J.MOLCATA.2007.08.023.
(58) Davó-Quiñonero, A.; Navlani-García, M.; Lozano-Castelló, D.; Bueno-López, A.; Anderson, J. A. Role of Hydroxyl Groups in the Preferential Oxidation of CO over Copper Oxide–Cerium Oxide Catalysts. *ACS Catal.* **2016**, *6* (3), 1723–1731. https://doi.org/10.1021/acscatal.5b02741.
(59) Davó-Quiñonero, A.; Navlani-García, M.; Lozano-Castelló, D.; Bueno-López, A. CuO/Cryptomelane Catalyst for Preferential Oxidation of CO in the Presence of H_2: Deactivation and Regeneration. *Catal. Sci. Technol.* **2016**, *6* (14), 5684–5692. https://doi.org/10.1039/C6CY00329J.
(60) Zasada, F.; Gryboś, J.; Indyka, P.; Piskorz, W.; Kaczmarczyk, J.; Sojka, Z. Surface Structure and Morphology of M[CoM′]O_4 (M = Mg, Zn, Fe, Co and M′ = Ni, Al, Mn, Co) Spinel Nanocrystals—DFT+U and TEM Screening Investigations. *J. Phys. Chem. C* **2014**, *118* (33), 19085–19097. https://doi.org/10.1021/jp503737p.
(61) Stelmachowski, P.; Zasada, F.; Maniak, G.; Granger, P.; Inger, M.; Wilk, M.; Kotarba, A.; Sojka, Z. Optimization of Multicomponent Cobalt Spinel Catalyst for N_2O Abatement

from Nitric Acid Plant Tail Gases: Laboratory and Pilot Plant Studies. *Catal. Letters* **2009**, *130* (3–4), 637–641. https://doi.org/10.1007/s10562-009-0014-z.

(62) Wang, H.-F.; Kavanagh, R.; Guo, Y.-L.; Guo, Y.; Lu, G.; Hu, P. Origin of Extraordinarily High Catalytic Activity of Co_3O_4 and Its Morphological Chemistry for CO Oxidation at Low Temperature. *J. Catal.* **2012**, *296*, 110–119. https://doi.org/10.1016/J.JCAT.2012.09.005.

(63) Nguyen, L.; Zhang, S.; Yoon, S. J.; Tao, F. F. Preferential Oxidation of CO in H_2 on Pure Co_3O_{4-x} and Pt/Co_3O_{4-x}. *ChemCatChem* **2015**, *7* (15), 2346–2353. https://doi.org/10.1002/cctc.201500320.

TOC Graphic

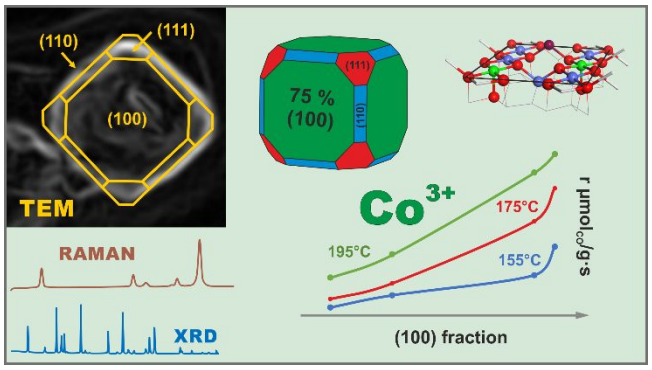
(110)
(111)
(100)
TEM
75 %
(100)
(111)
(110)
RAMAN
XRD
Co 3+
175°C
195°C
155°C
r /molCo/g.s
(100) fraction